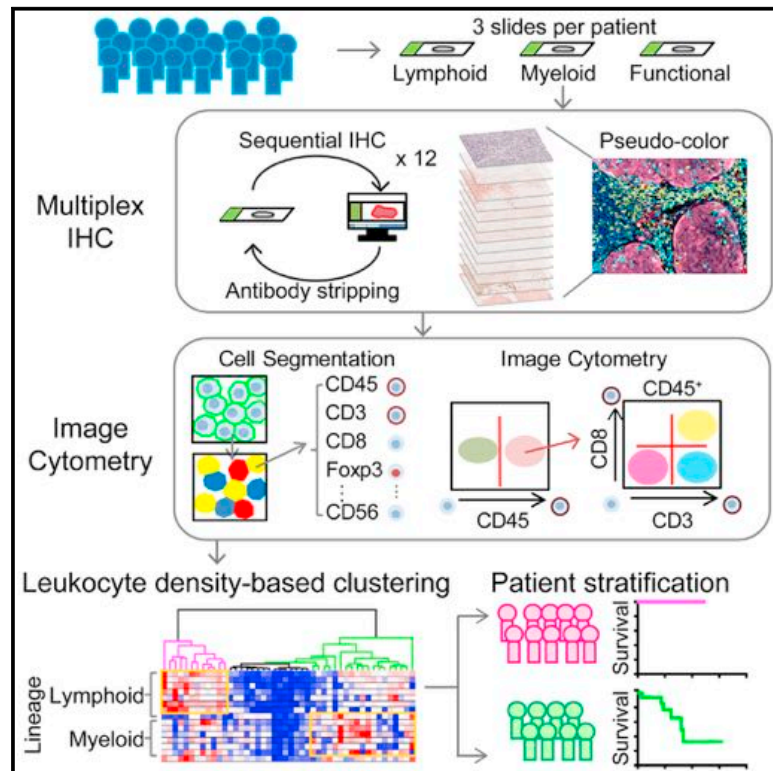


Cell Reports

Quantitative Multiplex Immunohistochemistry Reveals Myeloid-Inflamed Tumor-Immune Complexity Associated with Poor Prognosis

Graphical Abstract



Authors

Takahiro Tsujikawa, Sushil Kumar, Rohan N. Borkar, ..., Joe W. Gray, Paul W. Flint, Lisa M. Coussens

Correspondence

coussenl@ohsu.edu

In Brief

Tsujikawa et al. develop a multiplex immunohistochemistry and image cytometry platform to reveal immune-based metrics for patient stratification and response monitoring. In HNSCC and PDAC, prognosis correlates with mono-myelocytic cell density. In PDAC, percentages of PD-1, Eomes, Ki67, and granzyme B in CD8⁺ T cells correlate with response to vaccine therapy.

Highlights

- Multiplex IHC and computational image analysis phenotypes tumor-immune complexity
- In situ leukocyte density correlates with subclassification and prognosis in HNSCC
- Immune complexity stratifies response to vaccination therapy in PDAC
- CD8⁺ T cell and PD-L1 status correlate with outcomes of vaccinated PDAC patients



Quantitative Multiplex Immunohistochemistry Reveals Myeloid-Inflamed Tumor-Immune Complexity Associated with Poor Prognosis

Takahiro Tsujikawa,^{1,2} Sushil Kumar,¹ Rohan N. Borkar,¹⁰ Vahid Azimi,¹⁰ Guillaume Thibault,³ Young Hwan Chang,^{3,4} Ariel Balter,⁴ Rie Kawashima,¹ Gina Choe,¹ David Sauer,⁵ Edward El Rassi,² Daniel R. Clayburgh,^{2,9} Molly F. Kulesz-Martin,^{1,6,9} Eric R. Lutz,^{11,14,15} Lei Zheng,^{11,12,14,15} Elizabeth M. Jaffee,^{11,13,14,15} Patrick Leyshock,⁴ Adam A. Margolin,^{4,7,9} Motomi Mori,^{8,9} Joe W. Gray,^{3,7,9} Paul W. Flint,^{2,9} and Lisa M. Coussens^{1,9,16,*}

¹Department of Cell, Developmental & Cancer Biology

²Department of Otolaryngology-Head and Neck Surgery

³Department of Biomedical Engineering

⁴Department of Computational Biology

⁵Department of Pathology

⁶Department of Dermatology

⁷OHSU Center for Spatial Systems Biomedicine

⁸School of Public Health

⁹Knight Cancer Institute

Oregon Health and Science University, Portland, OR 97239, USA

¹⁰Intel Health and Life Sciences, Intel Corporation, Hillsboro, OR 97124, USA

¹¹Department of Oncology

¹²Department of Surgery

¹³Department of Pathology

¹⁴The Sidney Kimmel Cancer Center

¹⁵The Skip Viragh Center for Pancreatic Cancer Research and Clinical Care

Johns Hopkins University School of Medicine, Baltimore, MD 21205, USA

¹⁶Lead Contact

*Correspondence: cousseni@ohsu.edu

<http://dx.doi.org/10.1016/j.celrep.2017.03.037>

SUMMARY

Here, we describe a multiplexed immunohistochemical platform with computational image processing workflows, including image cytometry, enabling simultaneous evaluation of 12 biomarkers in one formalin-fixed paraffin-embedded tissue section. To validate this platform, we used tissue microarrays containing 38 archival head and neck squamous cell carcinomas and revealed differential immune profiles based on lymphoid and myeloid cell densities, correlating with human papilloma virus status and prognosis. Based on these results, we investigated 24 pancreatic ductal adenocarcinomas from patients who received neoadjuvant GVAX vaccination and revealed that response to therapy correlated with degree of mono-myelocytic cell density and percentages of CD8⁺ T cells expressing T cell exhaustion markers. These data highlight the utility of in situ immune monitoring for patient stratification and provide digital image processing pipelines to the community for examining immune complexity in precious tissue sections, where phenotype and tissue architecture are

preserved to improve biomarker discovery and assessment.

INTRODUCTION

Therapies targeting critical aspects of T cell regulation have revolutionized cancer therapy for some patients with highly antigenic cancer types (Palucka and Coussens, 2016); however, many patients still fail to respond and/or develop resistance to immune-based therapy. Moreover, tumors possessing low mutational burdens and/or those with limited antigenicity present unique therapeutic obstacles, because response rates for these remain low. Given that increased numbers of patients are now receiving some form of immune therapy, a major goal is to identify either in situ or circulating biomarkers to aid patient stratification for precision immune therapy such that efficacy can be increased and expanded across tumor types, as well as biomarkers for longitudinal response monitoring, e.g., remission and resistance.

Profiling immune contexture has emerged as a powerful metric for tumor subclassification, as well as predicting clinical outcome (DeNardo et al., 2011; Fridman et al., 2012; Galon et al., 2006; Ruffell et al., 2014; Zhang et al., 2003). Based on these insights, we predicted that effective auditing of tumor leukocyte biomarkers in situ might provide sufficient



stratification metrics with which to improve the success of immune-based therapies. A major obstacle for deployment of such a strategy is based on limited quantities of precious tumor-derived biopsy material for in situ prospective monitoring.

Herein we describe an optimized sequential immunohistochemistry (IHC) approach, using either biopsy or surgical specimens in formalin-fixed paraffin-embedded (FFPE) tissue sections and panels of antibodies enabling comprehensive phenotyping of immune complexity, together with computational image processing workflows that support a multiparameter cytometric quantification strategy. Altogether, these enable assessment of multiple lineage-selective and phenotypic biomarkers in three FFPE tissue sections quantitatively evaluated with three 12-antibody biomarker panels, which audit lymphoid and myeloid lineages, and the functional status of T cells.

Using this platform in a head and neck squamous cell carcinoma (HNSCC) cohort, we revealed that differential immune complexity, representing either lymphoid- or myeloid-inflamed tumors, correlated with clinical outcomes and tumor subclassification. In addition, by appending geometrical mapping analysis on top of leukocyte density, immune complexity status was linked to therapeutic response to vaccination therapy in pancreatic ductal adenocarcinoma (PDAC), where myeloid-inflamed and T cell exhaustion status correlated with shorter overall survival.

All required pipelines for digital image processing and related computational manuals are available at <https://github.com/multiplexIHC/cppipe>. Because this multiplex IHC platform is based on conventional digital IHC examination without requiring additional instrumentation, this method is technically and economically equivalent to standard IHC, thus enabling feasibility for large-scale studies without significant cost. These advancements will lead to expanding biomarker-based discovery and deployment in oncoimmunology research and improved ability to stratify and monitor patients receiving diverse immune-based therapeutics.

RESULTS

Optimized Sequential IHC and Digital Image Processing Enable Evaluation of 12 Biomarkers in One FFPE Tissue Section

To develop an IHC workflow enabling simultaneous evaluation of multiple biomarkers in one FFPE section, we built upon sequential IHC methodology originally reported for a 5-plex protocol (Glass et al., 2009) and subsequently expanded to enable 12-color sequential IHC with iterative labeling and stripping steps, facilitating analysis of more than 12 proteins on one tissue section, regardless of detecting antibody species of origin (Figures 1A, 1B, and S1). Briefly, after standard IHC preparation and primary antibody incubation, antibodies are detected by a F(ab') fragment-specific secondary antibody-labeled polymer-based peroxidase. Following detection, slides are visualized by alcohol-soluble peroxidase substrate 3-amino-9-ethylcarbazole (AEC), followed by whole-slide digital scanning. Iterative staining is achieved by AEC washing slides in ethanol (Glass et al., 2009; Tramu et al., 1978), followed by antibody stripping in heated citrate buffer (pH 6.0) (Lan et al., 1995). Slides are then washed and

equilibrated in binding buffer and readied for a subsequent round of primary antibody incubation. Complete stripping of antibodies and signals throughout all cycles was confirmed (Figure S2A). IHC sensitivity was equivalent to standard IHC throughout 11-repeated antibody-stripping rounds (Figures S2B and S2C).

After completing multiple rounds of sequential IHC, serially scanned and digitized images are processed with a computational image analysis workflow (see Supplemental Experimental Procedures). Briefly, sets of serial images are aligned based on a semi-automated coregistration pipeline using CellProfiler software as a backbone (Figure 1C) (Carpenter et al., 2006). Coregistered images are subsequently transferred to ImageJ (Schneider et al., 2012), and AEC and hematoxylin color information is extracted by color deconvolution algorithms (Ruifrok et al., 2003), wherein images are converted to grayscale and then visualized as pseudo-colored images (Figures 1D–1F).

Two 12-Biomarker Panels of Lineage-Selective Antibodies Identify and Phenotype Lymphoid and Myeloid Cells Evaluating Expression of 19 Distinct Biomarkers

To specifically audit complexity and phenotype of resident and infiltrating leukocytes in tumors in which geographic distribution can be preserved, we established two panels of 12 biomarkers each, encompassing 19 distinct epitopes to phenotype lymphoid and myeloid lineage cells (Figures 1A, 1B, 2, and S1; Table S1). The lymphoid biomarker panel depicts CD8⁺ T cells; T_H0, T_H1, T_H2, and T_H17 T cells; regulatory T cells (T_{REG}); B cells; and natural killer (NK) cells, while the myeloid biomarker panel visualizes CD163⁺ versus [−] tumor-associated macrophages (TAMs); immature (DC-SIGN⁺) versus mature (CD83⁺) dendritic cells (DCs); CD66b⁺ granulocytes (Gr), including neutrophils and eosinophils; and tryptase⁺ mast cells (Figures 2A, 2B, S1A, S1B, S3A, and S3B), thus enabling quantitative evaluation of 14 immune cell populations (Figure 2C).

Multiparameter Image Cytometry Enables Quantitative Assessment of 14 Cell Lineages in Multiplexed IHC Images

To enable quantitative evaluation of leukocyte features with regional and proximity analytics, we developed a multiparameter cytometric quantification approach via evaluation of single-cell-based chromogenic intensities using single-cell segmentation algorithms in CellProfiler (see Supplemental Experimental Procedures). We used hematoxylin-stained images for cell segmentation based on watershed algorithms (Padmanabhan et al., 2010; Wählby et al., 2004), followed by quantification of chromogenic signals in serial AEC-stained images, providing multiparametric information, including cell size, compactness, and location, with chromogenic intensity for each protein biomarker (Figure 3A). Single-cell-based information, including pixel intensity and shape-size measurements, was visualized and analyzed with qualitative assessment of signal intensities, analogous to flow cytometry (fluorescence-activated cell sorting [FACS]) data (Figure 3B). Thresholds for qualitative identification were determined based on distribution of plots for each marker in negative control slides (Figure S4A). Gated cells in dot plots were visualized in the original image, together with distribution

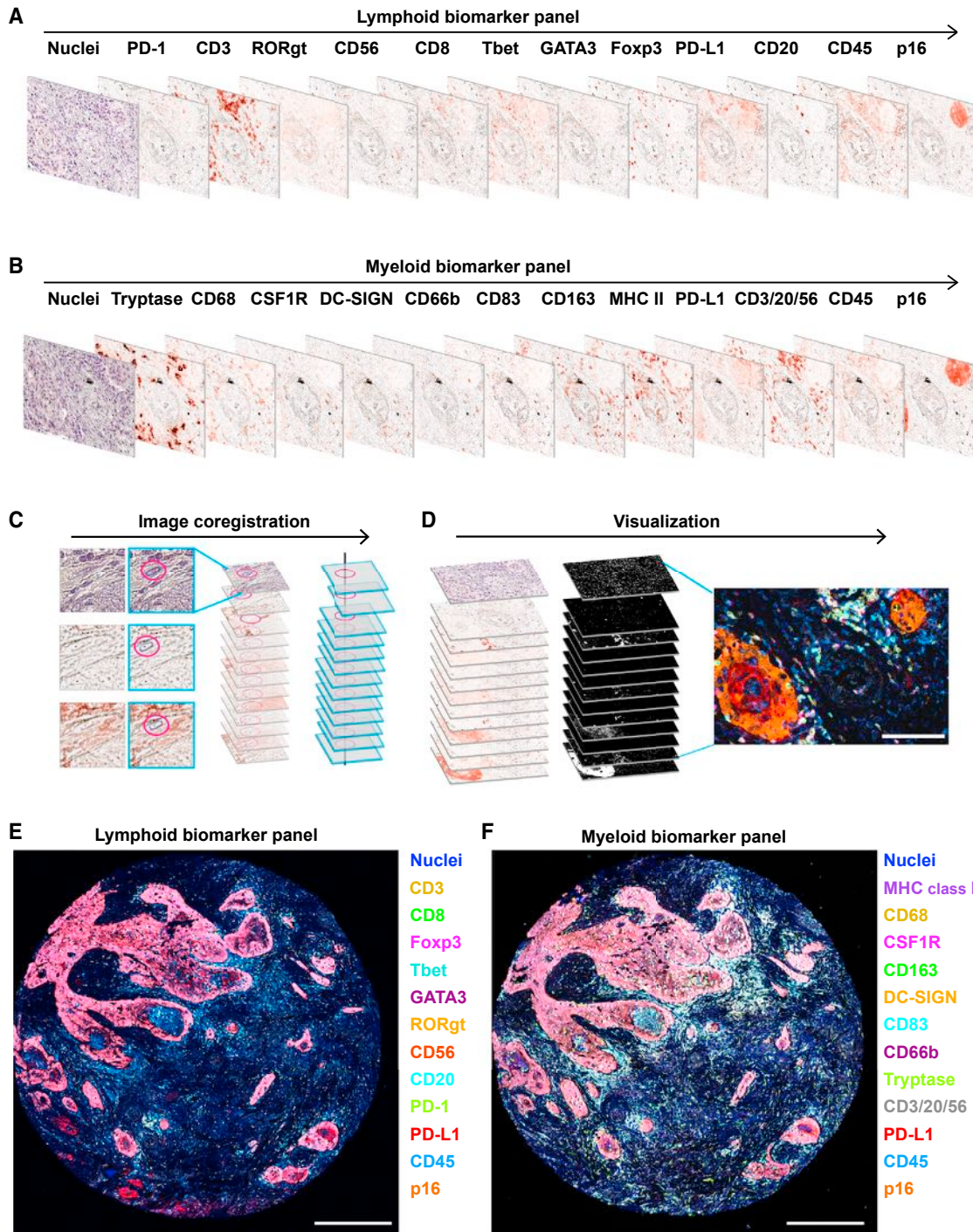


Figure 1. Schematic Overview of 12-Color Sequential IHC and Image Visualization

(A and B) Digital scans representing bright-field sequential IHC of one formalin-fixed paraffin-embedded (FFPE) section of human head and neck squamous cell carcinoma (HNSCC) tissue enable assessment of 12 lymphoid (A) and myeloid (B) biomarkers. Primary antibodies were visualized with horseradish peroxidase-conjugated polymer and 3-amino-9-ethylcarbazole (AEC) detection, followed by whole-slide digital scanning. Following destaining in an alcohol gradient and heat-based antibody stripping using citrate (pH 6.0) (see [Experimental Procedures](#) and [Table S1](#)), samples were restained sequentially with the indicated antibodies. (C) Following manual selection of a single cell or structure, indicated by magenta circles, the xy coordinates of scanned images were calculated and used for adjustment of alignment in CellProfiler (see [Experimental Procedures](#)).

(D) AEC color signals were extracted from each digitized single-marker image by color deconvolution, followed by pseudo-coloring. Scale bar, 100 μ m.

(E and F) Two serial FFPE sections of HNSCC were stained with the lymphoid (E) and myeloid (F) biomarker panels by pseudo-coloring. Biomarkers and colors are shown on the right. Corresponding single-marker images are shown in [Figures S1A](#) and [S1B](#). Scale bars, 500 μ m.

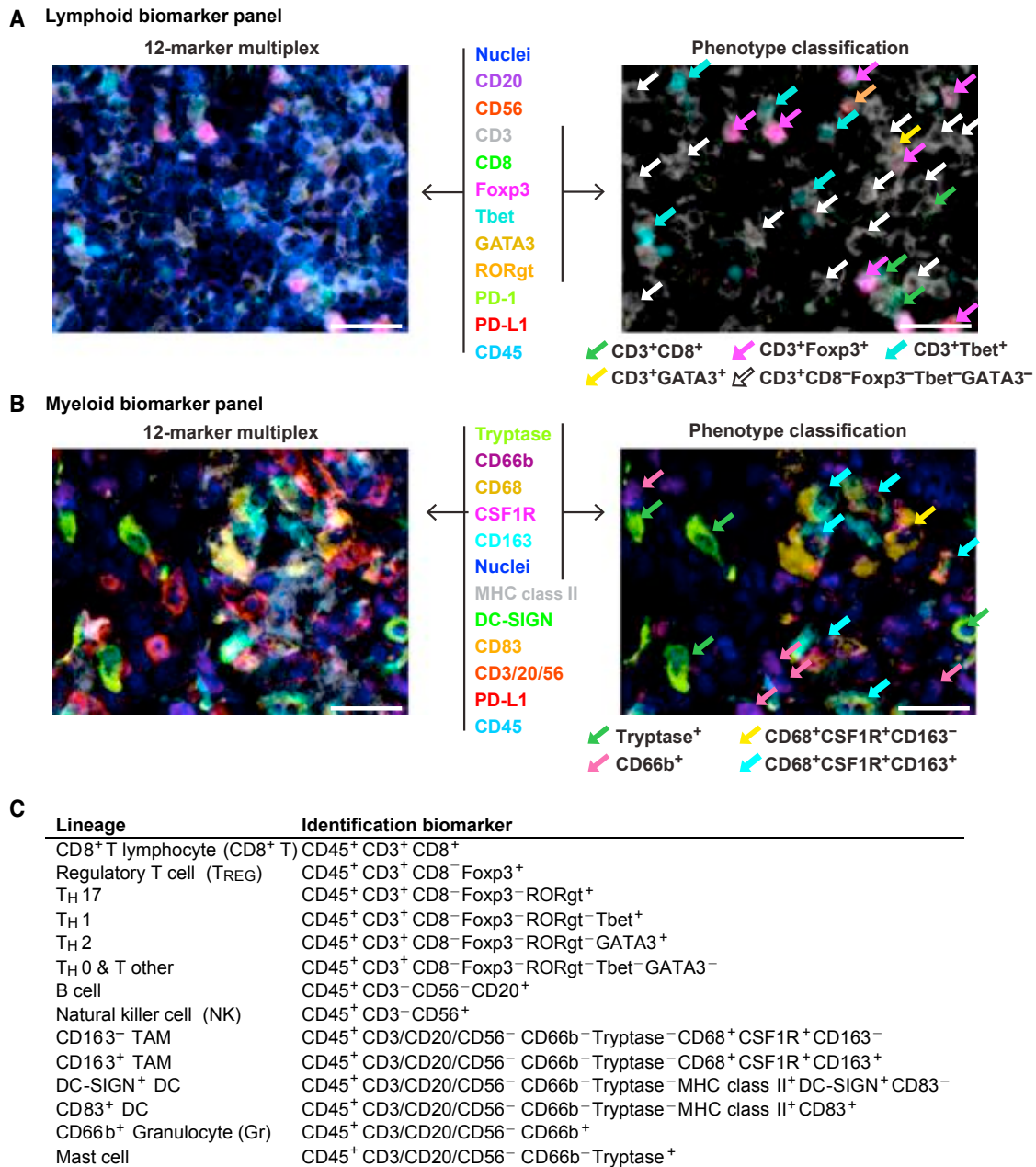


Figure 2. 12-Color Multiplex IHC to Visualize Lymphoid and Myeloid Immune Cell Phenotypes in FFPE Sections

(A and B) FFPE sections of human HNSCC tissues were analyzed by the two 12-marker panels of lineage-selective antibodies to identify lymphoid (A) and myeloid (B) lineages (left panels). Figure S3 shows single-color images for composites shown in (A) and (B). Colocalization of multiple markers enabled discernment of immune cell phenotypes, including CD3⁺CD8⁺ T cells; regulatory T cells (T_{REG}); T_H0, T_H1, T_H2, and T_H17 lymphocytes; CD163⁺ and CD163⁻ macrophages; CD66b⁺ granulocytes (Gr); and mast cells (right panels with colored arrows). Biomarkers and colors are shown in the center. Scale bars, 25 μm.

(C) Lineages and corresponding identification markers used in this study are shown.

in the tissue context, e.g., stromal versus within a neoplastic cell nest (Figure 3B). The xy coordinates of selected single cells were also depicted in the original image, enabling positioning of each cell in the corresponding image (Figure S4A).

To achieve quantitative data analogous to multiparametric 12-color FACS (Gunderson et al., 2016; Ruffell et al., 2012), we developed qualitative gating strategies for the panels (Fig-

ures 3C, 3D, and S4A–S4C). For comparative analyses between image cytometry and FACS, the same pieces of human surgical specimens were divided into two pieces, evaluated by single-cell suspension-based FACS analysis and FFPE section-based image cytometry, and observed for positive correlations in percentages of T and B cells measured by both methodologies (N = 9) (Figures S4D and S4E), (the

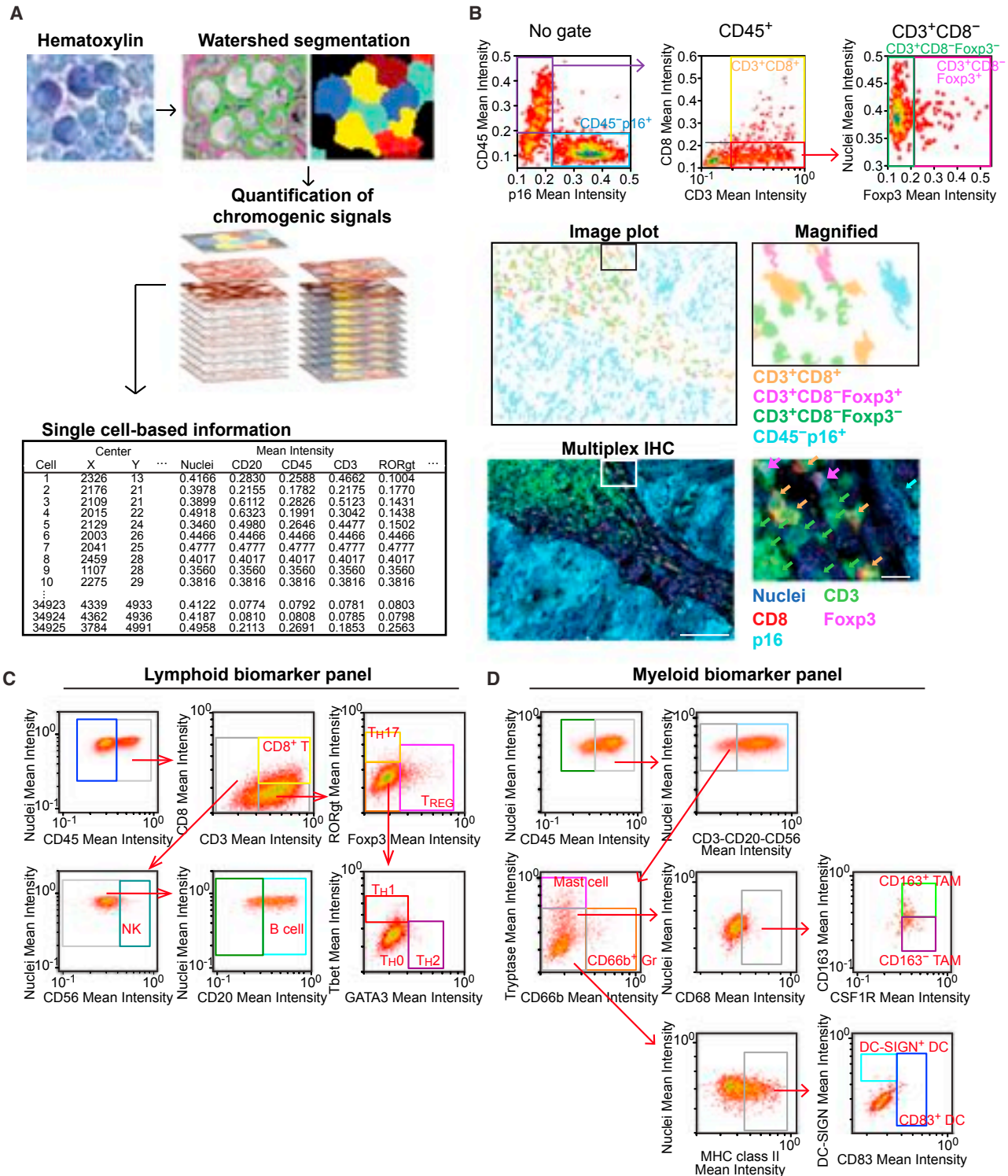


Figure 3. Multiparameter Cytometric Image Analysis for Quantification of Multiplex IHC

(A) A hematoxylin-stained image used for automated cell segmentation based on watershed segmentation algorithms by CellProfiler is shown (see [Experimental Procedures](#)). Segmentation results were used as templates for quantification of serially scanned AEC images, and pixel intensities of chromogenic signals and area-shape measurements were extracted and recorded by single-cell analysis, together with location in original images.

(B) Obtained single-cell-based chromogenic signal intensity, cell size or area, and location were used for density plots similar to flow cytometry by using the cytometry analysis software FCS Express 5 Image Cytometry (De Novo Software). Three dot plots shown at the top represent image cytometric analysis in (legend continued on next page)

Flow Repository: FR-FCM-ZY3A), thus validating the image cytometric approach.

In Situ Leukocyte Analysis Enables Tumor Subclassification and Risk Production in HNSCC

To verify the capability of the multiplex imaging and quantitation platform, we evaluated a tissue microarray (TMA) of oropharyngeal head and neck squamous cell carcinomas (HNSCCs), wherein the presence of oncogenic human papilloma virus (HPV) is associated with immunogenic gene signatures (Keck et al., 2014; Thurlow et al., 2010), thus serving as a validation control for the platform. A HNSCC TMA was assembled from 2 mm cores reflecting pathologist-selected representative intratumoral areas, including 21 HPV-positive and 17 HPV-negative tissues, with 8 non-malignant pharyngeal tissues (Table S2). IHC evaluation with lymphoid and myeloid panels was performed on two adjacent FFPE sections, wherein antibodies detecting p16 were included to assess HPV positivity (Figures 4A and 4B). Following quantification of cell densities and ratios of 14 immune cell lineages identified by image cytometry gating strategies (Figures 3C, 3D, S4B, and S4C), an unsupervised hierarchical clustering analysis was performed to identify distinct tumor subgroups based on immune complexity profiles (Figure 4C). This analysis revealed the presence of lymphoid-inflamed, hypo-inflamed, and myeloid-inflamed subgroups, wherein lymphoid and myeloid lineage cells were differentially present in stroma (Figures 4C and S5A). This observation was supported by cell density analyses among the three groups (Figure 4D). Using transversal quantification of multiple immune cell lineages, we evaluated ratios of CD8⁺ T cell to CD68 as IHC-based favorable predictors of clinical outcomes, as reported in other malignancies (DeNardo et al., 2011; Ruffell and Coussens, 2015), as well as CD163 expression on TAMs, which is associated with anti-inflammatory T_H2 phenotype and tumor initiation and progression (DeNardo et al., 2011; Mantovani et al., 2002). Although the hypo-inflamed group unsurprisingly revealed low scores, reflecting a “cold” inflammatory status, both ratios in the lymphoid-inflamed subgroup appeared significantly higher than those in the myeloid-inflamed subgroup (Figure 4E). In comparison, the myeloid-inflamed subgroup exhibited the shortest overall survival among the three subgroups, regardless of HPV status (Figures 4F and S5B). A leukocyte composition analysis of total CD45⁺ revealed high CD163⁻ and CD163⁺ TAMs and low T_H2 and B cells in HNSCC tissues in comparison to normal pharynx (Figure 4G). HPV-positive status was associated with high CD8⁺ T cells, while HPV-negative status correlated with high NK cells, DC-SIGN⁺ DCs, and CD66b⁺ Gr (Figure 4G), together indicating the presence of differential immune profiles between benign and malignant tissues, as well as HPV status. Distinct immune profiles depending on HPV status were also

confirmed by cell density-based analysis (Figure S5C). Results comparing HPV status were similarly observed by analysis of The Cancer Genome Atlas (TCGA) (Figure S5D), supporting validation of the method for evaluating HNSCC subtypes. To exclude potential bias from effects of differential tumor-stroma ratios on immune cell densities, we also evaluated tumor area percentage as a function of total tissue in each core and observed no significant differences among subgroups (Figures S5E and S5F). Although the lymphoid- and hypo-inflamed subgroups were clearly segregated between HPV-positive and HPV-negative status, respectively, the myeloid-inflamed subgroup with poor prognosis exhibited heterogeneity in HPV status (Figure 4C), indicating the possibility that further stratification of patients with HNSCC based on immune profiles beyond HPV status may be warranted. These data demonstrate that this quantitative imaging approach depicts distinct immune cell characteristics corresponding to tumor subtypes according to immune cell densities and HPV status associating with prognosis.

Differential Intratumoral Immune Complexity Stratifies Therapeutic Response to Neoadjuvant GVAX in Patients with PDAC

Based on the differential success of immune therapies using vaccines or therapeutic antibodies targeting costimulatory or coinhibitory molecules, we predicted that effective auditing of tumor leukocyte biomarkers might provide stratification metrics with which to improve success of these and other therapies. Thus, following validation of the multiplex imaging and quantitation approach using archival HNSCC, we sought to evaluate similar immune metrics to determine whether the approach would stratify patients based on therapeutic response to an immune therapy. To accomplish this, we used archival FFPE specimens from previously reported pancreatic ductal adenocarcinoma (PDAC) surgical specimens reflecting patients who received neoadjuvant GVAX therapy, a granulocyte-macrophage colony-stimulating factor (GM-CSF)-secreting pancreatic tumor vaccine (NCT: NCT00727441) (Lutz et al., 2014), in which intratumoral lymphoid aggregates develop in some patients as a post-vaccination response (Table S3). Adjacent FFPE tissues sections were stained using the lymphoid-selective and myeloid-selective antibody panels (Figures 5A, S6A, and S6B) and quantitatively evaluated by image cytometry (Figures S6C and S6D) in three areas per FFPE tissue (Figures S6E and S6F) that typically included lymphoid aggregate regions (Figure 5A). The three 25-megapixel images (approximately 2.5 × 2.5 mm square) were selected as regions of interest (ROIs) based on geometrical mapping analyses of CD45⁺ leukocyte cell densities (see Experimental Procedures; Figure S9). Following an unsupervised hierarchical clustering analysis similar to Figure 4C,

a p16⁺ HNSCC tissue. Gated cell populations of CD45⁺CD3⁺CD8⁺ T cells, CD45⁺CD3⁺CD8⁻ Foxp3⁺, CD45⁺CD3⁺CD8⁻ Foxp3⁻, and CD45⁻p16⁺ cells are shown (middle) as an image plot with coloring of orange, magenta, green, and cyan, respectively. A five-color multiplex IHC image corresponding to the image plot is shown at the bottom, revealing matched identification between image cytometry and visualized images. The boxes depict magnified areas. Scale bars, 100 μm (low magnification) and 10 μm (high magnification).

(C and D) Image cytometry-based cell population analyses for the lymphoid and myeloid biomarker panels are shown in (C) and (D), respectively. The markers used for identification of cell lineages are shown in Figure 2C. Gating thresholds for qualitative identification were determined based on data in negative controls (Figures S4B and S4C). The x and y axes are shown on a logarithmic scale.

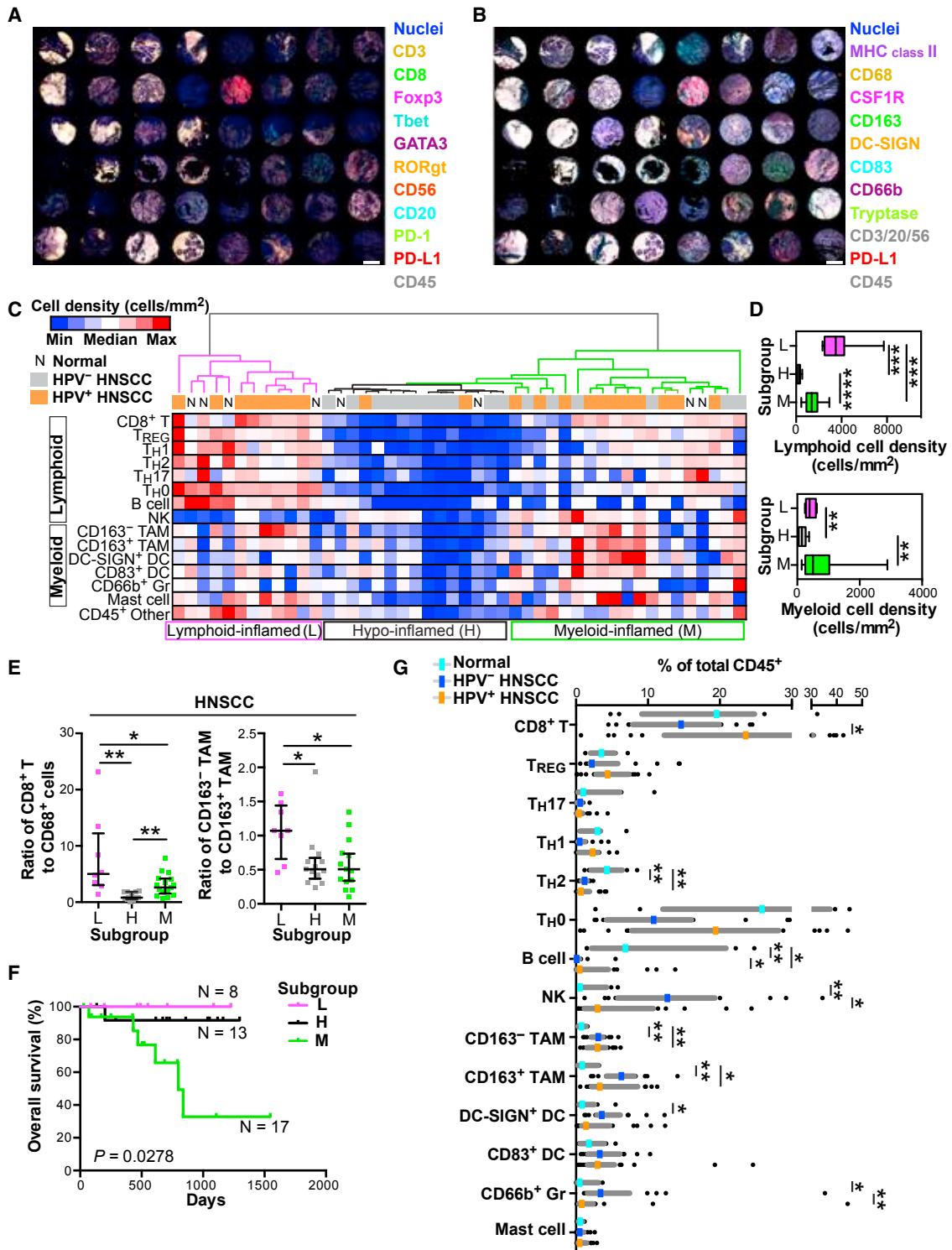


Figure 4. Quantitation of Immune Cell Density-Based Subgrouping Enables Stratification for Prognosis and HPV Status in HNSCC

(A and B) Two FFPE sections from a HNSCC-assembled TMA, including both HPV-negative (n = 17) and HPV-positive (n = 21) oropharyngeal tumor and normal oropharynx (n = 8), were stained using the lymphoid (A) and myeloid biomarker antibody panels (B). Scale bar, 1.0 mm.

(C) Cell densities (in cells per square millimeter) of 15 immune cell lineages in each core were quantified using image cytometry. Datasets from the two panels reflecting lymphoid and myeloid biomarkers were normalized based on CD45⁺ cell number. A heatmap according to color scale (upper left) is shown with

(legend continued on next page)

we observed differential immune complexity profiles showing low and high myeloid-inflamed status (Figure 5B). The two clusters showed differential myeloid cell densities, but not lymphoid cell densities (Figure 5C), compatible with robust induction of lymphoid aggregate regions post-GVAX. However, despite relatively high lymphoid cell densities in both groups, the existence of immunosuppressive profiles dominated the high myeloid-inflamed group, based on ratios of CD8⁺ T cells to CD68⁺ cells and T_H2 polarization of CD8⁻ T cells (Figures 5D and S6G). Comparison of these results associated with immunosuppressive status, and the high myeloid-inflamed group was associated with short overall survival based on Kaplan-Meier analysis (Figure 5E). Altogether, these results support the hypothesis that intratumoral leukocyte analysis, and specifically a myeloid-inflamed stroma, may limit efficacy of GVAX therapeutic responses despite successful induction of lymphoid infiltration.

CD8⁺ T Cell Status Correlates with Myeloid Inflammation and Reflects Outcome in Response to GVAX Therapy

Because tumor-associated myeloid populations contribute to cancer progression based partly on their immunosuppressive capabilities regulating T cell dysfunction (Paley et al., 2012; Twyman-Saint Victor et al., 2015; Wherry and Kurachi, 2015), e.g., proliferation (DeNardo et al., 2011; Ruffell et al., 2014), recruitment (Affara et al., 2014), differentiation, and effector function (Gunderson et al., 2016; Mantovani et al., 2002; Palucka and Coussens, 2016), we sought to integrate in situ assessment of T cell functional status as related to myeloid versus lymphoid status of tumors. To achieve this, we developed a third antibody panel (Figures 6A and S7A) for multiplex IHC (Figures 6B and S7B), in combination with quantitative image cytometry (Figure 6C), to examine T cell activation or exhaustion status in the same three tissue areas analyzed for lymphoid and myeloid complexity (Figure 5A). Images were quantitatively evaluated by image cytometry; further dissection was then based on CD45⁺CD3⁺CD8⁺ T cells expressing the coinhibitory receptor programmed cell death-1 (PD-1), effector T cell development-associated Eomesodermin (Eomes), and followed by assessment of proliferation (Ki67) and cytotoxic (granzyme B) activity (Figures 6C–6F, S7C, and S7D). Comparative analysis between the low and the high myeloid-inflamed profiles observed in Figure 5B revealed that high myeloid profiles correlated with PD-1⁺Eomes⁺ CD8⁺ T cells linked to an exhausted phenotype (Twyman-Saint Victor et al., 2015; Wherry and Kurachi, 2015), together with expansion of PD-1⁻Eomes⁺ late effector T cells (Figure 6D). The expanded PD-1⁺Eomes⁺ CD8⁺ T cell component in the myeloid-inflamed group exhibited relatively low

Ki67 expression, further indicating the presence of exhausted T cells in relation to myeloid lineage enrichment (Figures 6D and S7C). Further analysis of the prognostic impact of in situ T cell functional status revealed that short overall survival was associated with low proliferation status of CD8⁺ T cells (Figures 6E and S7D), as well as low activation status assessed by granzyme B (Figure 6F). Altogether, these data indicate that myeloid-dominated immune environments associate with restricted T cell functionality, regardless of the degree of lymphoid inflammation, and adversely correlate with clinical outcome following neoadjuvant GVAX therapy.

Myeloid PD-L1 Correlates with Activated CD8⁺ T Cell Status, Associated with Favorable Prognosis following GVAX

Considering these data revealed the significance of understanding T cell activation or exhaustion status in the context of myeloid-mediated inflammation, that expression of programmed cell death-1 ligand (PD-L1) on myeloid cells may provide prognostic information for therapeutic response to immune therapy (Parsa et al., 2007; Patel and Kurzrock, 2015; Topalian et al., 2012), and that blockade of the PD-1/PD-L1 axis reflects a therapeutic strategy for HNSCC and PDAC (Paley et al., 2012; Topalian et al., 2012), we sought to examine PD-L1 expression in relation to T cell functional status to assess its biomarker potential for patient stratification using both the HNSCC and the PDAC samples evaluated earlier.

In the HNSCC TMA (Figure 4), 6 of 38 cases exhibited diffuse PD-L1 expression in HNSCCs (Figure S8A), where PD-L1 expression was observed in a spectrum of leukocyte lineages, including CD163⁺ and CD163⁻ TAMs, CD83⁺ and DC-SIGN⁺ DCs, NK cells, CD66b⁺ Gr, mast cells, T cells, and B cells (Figure S8B), in agreement with previous reports (Lyford-Pike et al., 2013; Pardoll, 2012; Soares et al., 2015). To quantitatively verify these observations, the positive percentage of PD-L1 expression in each cell lineage was then quantified by image cytometry and transversely analyzed across cell lineages, together with subclassification of tumor or normal tissue types. Among cell lineages including CD45⁻ neoplastic cells, the highest frequency of PD-L1 expression was observed on myeloid cells (Figure S8C). High PD-L1 expression on myeloid cells was observed particularly in HPV-associated tumors (Figure S8C), associated with lymphoid-inflamed profiles (Figure 4C).

In the GVAX-treated PDAC samples (Figure 5), PD-L1 expression was identified predominantly in CD45⁺ cells and particularly in CD68⁺ and major histocompatibility complex class II-positive (MHC class II⁺) cells and DCs, rather than CD45⁻ populations (Figures 7A and 7B). To investigate a potential association

a dendrogram of unsupervised hierarchical clustering, depicting lymphoid-, hypo-, and myeloid-inflamed subgroups (L, H, and M at the bottom, respectively). See also Figure S5C and Table S2.

(D) Immune cell densities of lymphoid and myeloid cell lineages comparing subgroups in (C). Bars, boxes, and whiskers represent median, interquartile range, and range, respectively.

(E) Ratios of cell percentages comparing subgroups are shown. Bars show median with interquartile range.

(F) Kaplan-Meier analysis of overall survival of HNSCC patients stratified by subgroups. Statistical significance was determined via log-rank test.

(G) Immune cell percentages were quantified as a percentage of total CD45⁺ cells. Vertical lines and gray bars show median and interquartile range, respectively. Statistical differences in (D), (E), and (G) were determined via Kruskal-Wallis tests with false discovery rate (FDR) adjustments, with *p < 0.05, **p < 0.01, ***p < 0.001, and ****p < 0.0001.

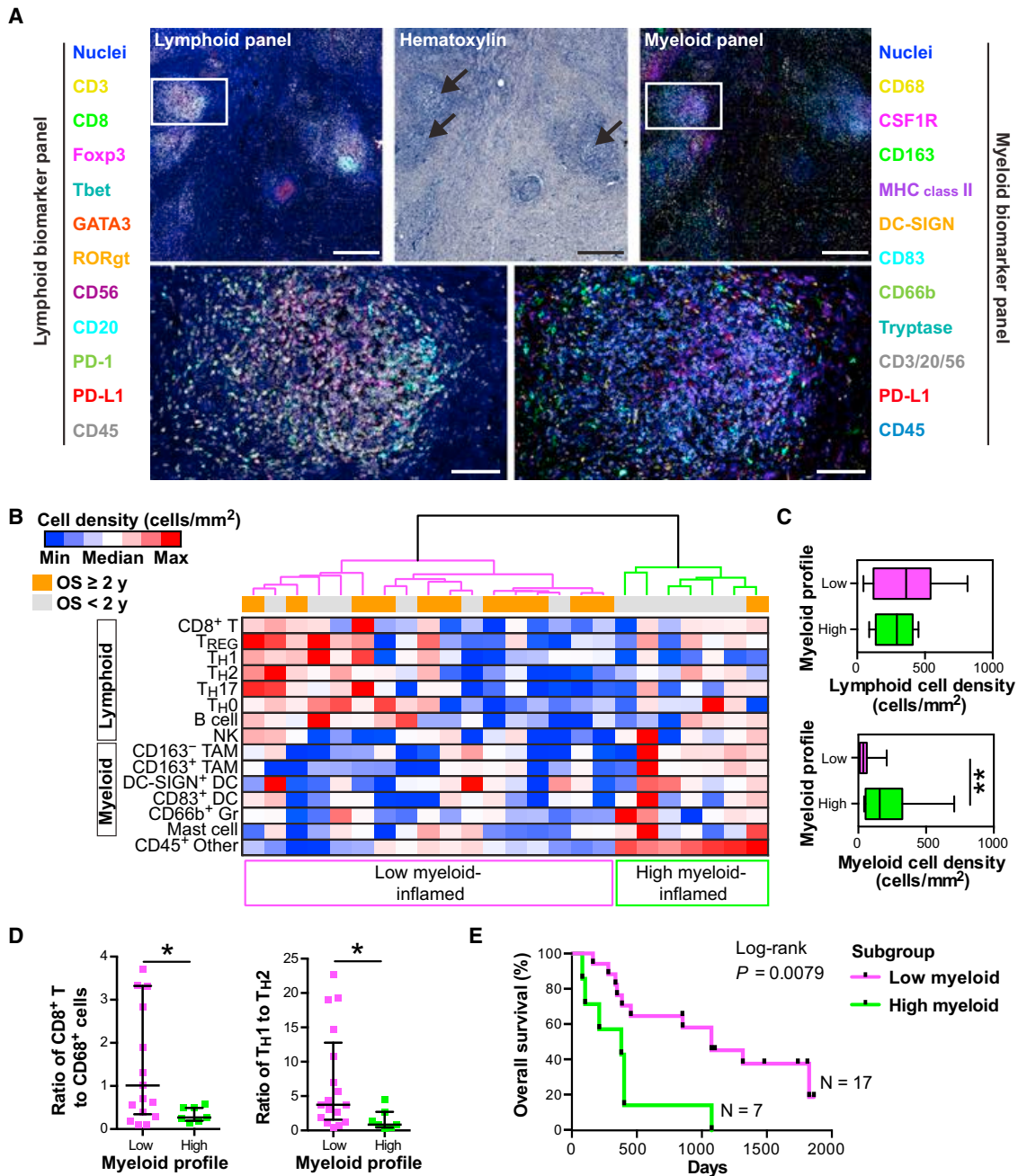


Figure 5. Immune Complexity Correlates with Therapeutic Response to Neoadjuvant GVAX Therapy in PDAC

(A) Two adjacent FFPE sections from human PDAC tissues derived from neoadjuvant GVAX-treated individuals (N = 24) (Table S3) were analyzed by multiplex IHC. Representative 12-color composite images of myeloid and lymphoid biomarker panels are shown with a corresponding hematoxylin image. Biomarkers and colors are shown. The boxes represent the magnified area below. Scale bars, 500 μ m (low) and 100 μ m (high magnification). Corresponding single-marker images are shown in Figures S6A and S6B.

(B) Immune cell densities (in cells per square millimeter) of three leukocyte hotspots in intratumoral regions (see Figure S6E) were assessed by multiplex IHC and image cytometry in analogs to Figure 4C. A heatmap according to color scale (upper left) is shown with a dendrogram of unsupervised hierarchical clustering, depicting low and high myeloid-inflamed subgroups.

(C) Immune cell densities of lymphoid and myeloid cell lineages comparing subgroups in (B). Bars, boxes, and whiskers represent median, interquartile range, and range, respectively.

(D) Ratios of cell percentages comparing subgroups are shown. Bars show median with interquartile range.

(E) Kaplan-Meier analysis of neoadjuvant GVAX-treated PDAC cohort (N = 24) stratified by subgroups.

Statistical significance in (E) was determined via log-rank test. Statistical differences in (C) and (D) were determined via Kruskal-Wallis tests, with * $p < 0.05$ and ** $p < 0.01$.

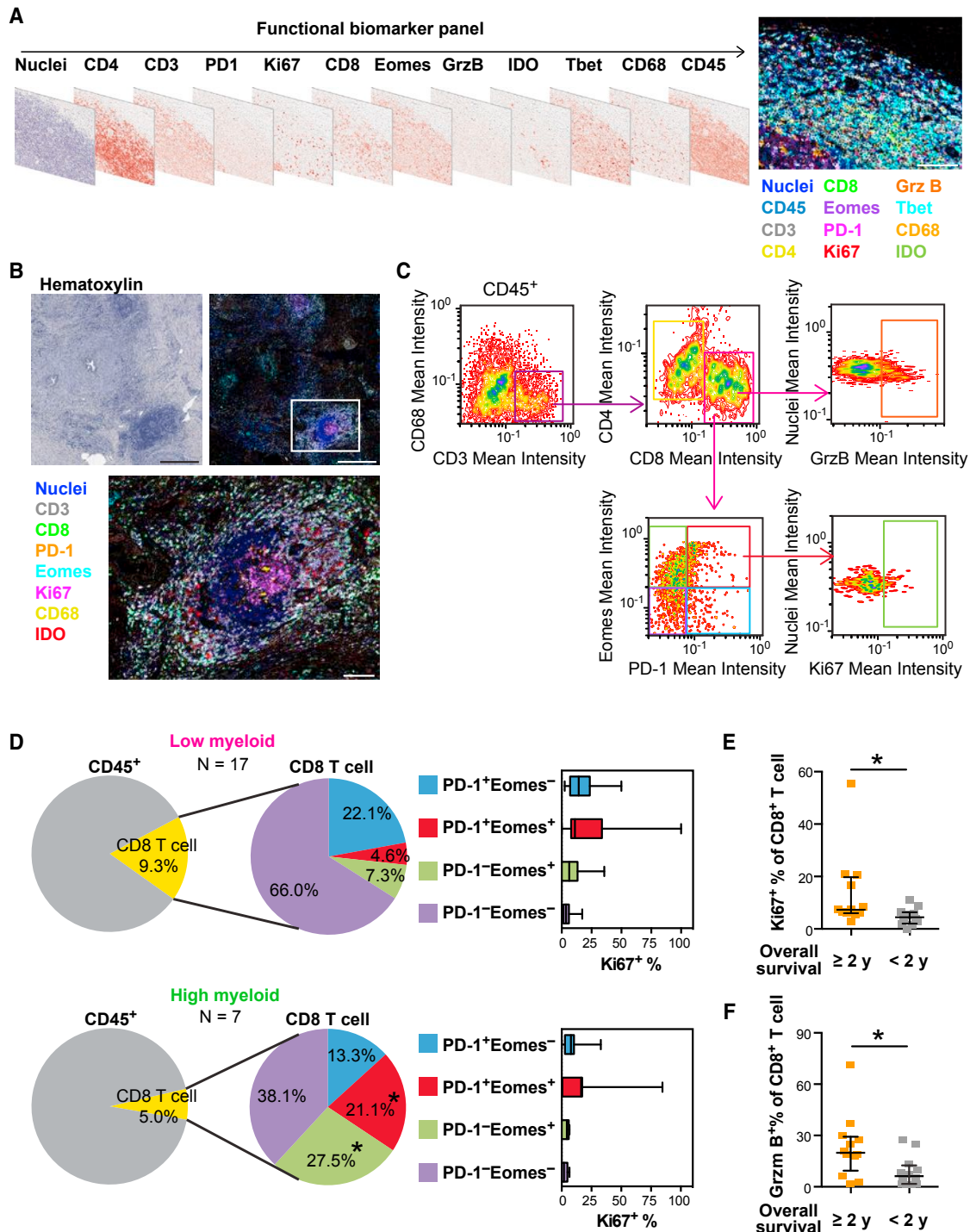


Figure 6. In Situ T Cell Functional Biomarker Assessment Elucidates CD8⁺ T Cell Status in Non-responders to Neoadjuvant GVAX Treatment

(A) T cell functional biomarker panel is shown as digital scans of bright-field sequential IHC derived from a single FFPE section of human tonsil tissue. Scale bar, 100 μ m. Corresponding single-marker images are shown in Figure S7A.

(B) Representative images from PDAC tissue, including lymphoid aggregates. Biomarkers and colors are shown. Boxes represent the magnified area below. Scale bars, 500 μ m (low) and 100 μ m (high magnification). See also Figure S7B.

(C) Gating strategy for image cytometry of the T cell functional biomarker.

(D) CD8⁺ T cells in neoadjuvant GVAX-treated PDAC tissues (N = 24) were assessed by T cell functional biomarker panel in three regions per tissue matched to analyzed regions in Figure 5C. Left pie charts represent average of CD8⁺ T cell percentages of total CD45⁺ cells, comparing low and high myeloid-inflamed

(legend continued on next page)

between T cell functional status and PD-L1, we examined the T cell activation marker granzyme B and observed a significant correlation with PD-L1⁺ cells (Figures 7C and 7D) independent of CD8⁺ T cell frequency (Figure S8D). This observation was supported by analysis of granzyme B⁺CD8⁺ T cell density (Figure S8E). Furthermore, as was observed in Figure 7A, PD-L1 expression on CD163⁺ TAMs and DC-SIGN⁺ immature DCs correlated with granzyme B positivity of CD8⁺ T cells (Figures 7B and S8F). As expected, high PD-L1 expression on myeloid cells was associated with high granzyme B expression in CD8⁺ T cells, indicating a correlation between PD-L1 upregulation and activated T cell status. Because activated T cell status was linked to favorable prognosis (Figure 6F) and high PD-L1 expression was observed on myeloid lineages (Figure 7B), we then evaluated prognostic significance of myeloid PD-L1 based on Kaplan-Meier analyses, revealing that high PD-L1 expression on myeloid lineages represented by MHC class II⁺ cells and CD68⁺ cells indicated significantly longer overall survival (Figures 7E and 7F). Given that PD-L1 plays a physiological function for auto-regulatory immune mechanisms, altogether these results imply that upregulated PD-L1 on myeloid cells could be a result of phenotypic changes in response to abundant inflammatory cytokines following successful induction of lymphoid-inflamed profiles. Simultaneously, these observations indicate that PD-L1 expression on myeloid cells potentially serves as a biomarker for vaccination therapy, as well as therapeutic targets via immune checkpoint blockade.

DISCUSSION

In this study, we investigated tumor immune characteristics of archival HNSCC tumors and in PDAC specimens from patients who had received neoadjuvant GVAX therapy, using a multiplex IHC methodology optimized for immune complexity and phenotype analyses and accompanied by quantitative studies using a computational image processing workflow. The imaging approach and analysis pipeline enable quantitative assessment of immune infiltrates based on sequential IHC using FFPE specimens to identify clinical correlations for patient stratification.

The three antibody panels described herein enable simultaneous evaluation of leukocyte presence, complexity, and functional status in a variety of FFPE tissue contexts. In addition to the HNSCC and PDAC evaluated herein, this platform has been used for quantitative assessment of papillary thyroid carcinomas and longitudinal core biopsy samples of mesothelioma and breast and pancreas tumors from patients receiving various regimens of immune therapy (data not shown), as well as murine tissues and tumors (Gundersen et al., 2016; Liu et al., 2017), thus revealing the broad applicability of the approach using minimal FFPE tissue sections. Considering that FFPE sections are widely used for routine preparation of diagnostic pathology, this

method accelerates retrospective biomarker studies in archival tissue sections, as well as prospective and longitudinal assessment using core biopsy specimens to monitor response.

Although current gene expression-based profiling is not capable of assessing single-cell-based phenotypes or retention of tissue context information, our approach described herein circumvents these issues. However, one possible limitation is a lack of direct correlation between protein expression level and signal intensity; chromogenic amplification provides non-linear correlation with protein expression levels. To compensate for this issue, we adopted thresholding approaches to identify positive and negative cell populations based on qualitative gating, in which thresholds were determined by basic signal intensities in negative controls (Figures S4A–S4C). Based on this qualitative gating strategy, we observed that image cytometry and flow cytometry data performed similarly in quantification of lymphocytes (Figure S4E); thus, this imaging approach serves as a platform to perform multiparametric assessment of various cell lineages, enabling tumor localization information. Although this method enables lineage identification based on multiple lineage-selective markers (Figure 2), because specific cell types have a great diversity with regards to lineage-restricted biomarkers, an ultimate classification of leukocyte subsets based on markers used herein remains limited and awaits further technological and bioinformatic innovations.

Analysis of the archival HNSCC cohort described herein supports the notion that immune complexity of HNSCC reflects clinical outcome and tumor-molecular phenotype, including the presence of viral antigens. In comparison with previous reports revealing that malignancies associated with oncogenic viruses typically induce viral antigen-specific CD8⁺ T cells infiltration (Gentles et al., 2015), the multiplex platform affirmed that HPV-associated HNSCCs contain significantly higher CD8⁺ T cell densities and, together with other T_H1-associated immune infiltrates such as Tbet⁺ T_H1 cells and CD163[−] TAMs (Figure 4G), indicates the presence of anti-tumor immunoreactivity, possibly against HPV antigens. However, immune cell complexity profiles of HNSCC revealed lymphoid-inflamed, myeloid-inflamed, and hypo-inflamed signature-based subtypes not previously identified by gene expression analyses, in which myeloid-enriched T_H2-biased tumors were associated with decreased overall survival (Figure 4C–4F). Although there were clear tendencies of lymphoid-inflamed tumors correlating with HPV-positive tumors, a portion of HPV-positive tumors also correlated with myeloid-inflamed profiles, and these associated with poor prognosis (Figure 4C), potentially indicating association between myeloid-driven tumor characteristics and disease aggressiveness. Altogether, these observations indicate that tumor characteristics affect infiltration and phenotypes of tumor-infiltrating immune cells, simultaneously confirming the capability of this intratumoral in situ imaging approach.

profiles defined in Figure 5C. Middle pie charts give average percentages, showing a composition of CD8⁺ T cells stratified by PD-1 and Eomes expression. Box whisker plots at the right show Ki67⁺ percentages evaluated in each CD8⁺ T cell subpopulation. Bars, boxes, and whiskers represent median, interquartile range, and range, respectively. Statistical significances between the two groups were determined via Kruskal-Wallis tests with FDR adjustments, with **p* < 0.05. (E and F) Percentages of Ki67 (E) and granzyme B (F) in CD8⁺ T cells in neoadjuvant GVAX-treated PDAC tissues are shown, comparing overall survival ≥ 2 years (*n* = 12) and overall survival < 2 years (*n* = 12). Bars show median with interquartile range. Statistical significances were determined via Kruskal-Wallis tests, with **p* < 0.05.

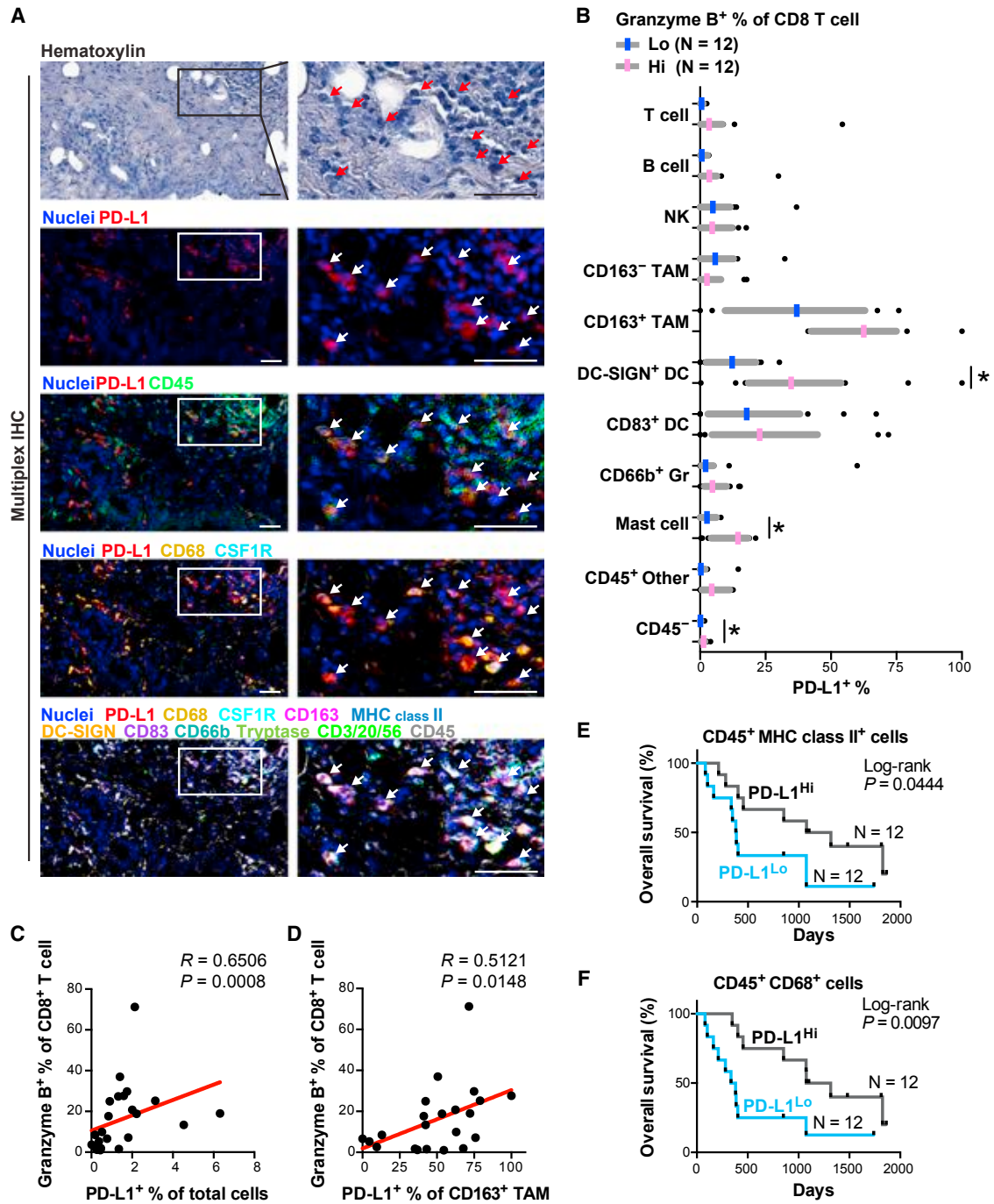


Figure 7. Myeloid PD-L1 Expression Correlates with Favorable Prognosis following Neoadjuvant GVAX Treatment and Associates with CD8⁺ T Cell Activation Status

(A) Multiplex IHC images showing PD-L1 expression in neoadjuvant GVAX-treated PDAC tissues. Arrows depict PD-L1⁺ cells, demonstrating colocalization with CD45⁺ CD68⁺ CSF1R⁺ macrophages. Scale bars, 100 μ m.

(B) PD-L1⁺ percentages were assessed in the cell lineages shown, comparing low (n = 12) and high (n = 12) groups in granzyme B percentages of CD8⁺ T cells. Median (11.7%) was used for the cutoff line of granzyme B status. Three regions per tissue matched to analyzed regions in Figure 5C were evaluated. Vertical lines and gray bars show median and interquartile range, respectively. Statistical significances were determined via Kruskal-Wallis tests with FDR adjustments, with *p < 0.05.

(C and D) Spearman correlations of granzyme B⁺ percentages of CD8⁺ T cells versus PD-L1⁺ percentages of total cells (C) or CD163⁺ tumor-associated macrophages (TAMs) (D) are shown with estimated regression lines (red) in the neoadjuvant GVAX-treated PDAC cohort (N = 24).

(E and F) Kaplan-Meier analyses of neoadjuvant GVAX-treated PDAC stratified by PD-L1⁺ percentages in CD45⁺ CD68⁺ cells (E) and CD45⁺ MHC class II⁺ cells (F). Median (15.7% and 18.7%) was used for the cutoff line of PD-L1 status (for E and F, respectively). Statistical significance was determined via log-rank test.

Similar to findings in HNSCC, regardless of lymphoid lineage quantity in PDAC specimens, myeloid-enriched immune profiles associated with T_H2-driven phenotypes and poor prognosis in response to neoadjuvant GVAX vaccination therapy (Figures 5B–5E), again indicating that myeloid enrichment negatively affects anti-tumor immune responses as predicted by numerous murine modeling studies (DeNardo et al., 2011; Mantovani et al., 2002; Ruffell et al., 2010, 2014; Ruffell and Coussens, 2015). Quantitative evaluation of functional indicators of T cell differentiation, proliferative, and effector status supported these observations in revealing that myeloid-inflamed tumors correlated with shortened survival and were linked to CD8⁺ T cell exhaustion status, e.g., low Ki67 and granzyme B expression (Figures 6D–6F). Conversely, activated CD8⁺ T cell status correlated instead with high PD-L1 expression on myeloid cells, as well as favorable prognosis (Figures 7E and 7F), indicating the importance of understanding total immune complexity and phenotype originating from both lymphoid and myeloid lineages. Altogether, data revealed from PDAC and HNSCC specimens through multiplex IHC and computational image processing analysis support the tenant that immune contexture can be effectively used as a metric for predicting clinical outcomes and responses to therapy. Results described herein also reveal characteristics of myeloid lineages whose presence in tumors restricts induction of anti-tumor immunity and thus highlight the therapeutic potential for select myeloid antagonists, in combination with vaccine and/or checkpoint-targeted immune therapy.

EXPERIMENTAL PROCEDURES

Clinical Samples and TMA Construction

FFPE surgical specimens from 38 patients with previously untreated oropharyngeal squamous cell carcinoma were obtained from the Oregon Health and Science University (OHSU) Knight Biobank and the OHSU Department of Dermatology research repository and were used to create a TMA. Cohort characteristics of HNSCC are shown in Table S2. A total of 24 human PDAC tumor specimens with the presence of intratumoral lymphoid aggregates were obtained from our previous study, wherein allogeneic GM-CSF-secreting pancreatic tumor vaccine (GVAX) was administered intradermally either alone or in combination with immune modulatory doses of cyclophosphamide as neoadjuvant treatment for patients with resectable PDAC (NCT: NCT00727441) (Table S3) (Lutz et al., 2014). Further details can be found in Supplemental Experimental Procedures.

Sequential IHC and Image Acquisition

Chromogenic sequential IHC was conducted with 5 μm of FFPE tissue sections. Following deparaffinization, slides were stained by hematoxylin (S3301, Dako) for 1 min, followed by whole-tissue scanning using Aperio ImageScope AT (Leica Biosystems). Slides were subjected to endogenous peroxidase blocking followed by heat-mediated antigen retrieval. Then, sequential IHC consisting of iterative cycles of staining, scanning, and antibody and chromogen stripping was performed according to a modified protocol based on previous reports (Glass et al., 2009; Lan et al., 1995; Tramu et al., 1978). Primary antibodies, horseradish peroxidase (HRP)-conjugated polymer, and chromogenic detection were serially added in the indicated order and condition shown in Table S1. Two forms of negative controls were used during analyses; slides for conventional negative controls were treated with 2.5% goat serum in PBS without primary antibodies; slides for sequential IHC negative controls were used for confirmation of complete antibody and signal stripping (Figure S2A). Further details can be found in Supplemental Experimental Procedures.

Image Processing and Analysis

The digital image workflow encompasses three steps: image preprocessing, visualization, and quantitative image analysis, as shown in Supplemental Experimental Procedures. In image preprocessing, iteratively digitized images were coregistered so that cell features overlap down to a single-pixel level, using a CellProfiler v.2.1.1 pipeline, Alignment_Batch.cppipe (available under General Public License version 2 [GPLv2] at <https://github.com/multiplexIHC/cppipe>). Pseudocodes for algorithms used are available in Supplemental Experimental Procedures. In the PDAC surgical specimen analysis, a heatmap of CD45⁺ cell density was used for selection of three rectangle ROIs within an intratumoral high CD45-density area (approximately 6.25 mm², or less if the analyzable cancerous area is smaller than 3.0 × 6.25 mm²) (Figure S6F). Visualization was performed via conversion of coregistered images to pseudo-colored single-marker images in ImageJ v.1.48 (Schneider et al., 2012) and ImageScope (Leica Biosystems). In quantitative image assessment, single-cell segmentation and quantification of staining intensity were performed using a CellProfiler v.2.1.1 pipeline, CellID_FlowCyt-6.9.15.cproj (available under GPLv2 at <https://github.com/multiplexIHC/cppipe>). Pseudocodes for algorithms used are available in Supplemental Experimental Procedures. All pixel intensity and shape-size measurements were saved to a file format compatible with flow and image cytometry data analysis software, FCS Express 5 Image Cytometry v.5.01.0029 (De Novo Software). Further details can be found in Supplemental Experimental Procedures.

Flow Cytometry

Flow cytometry studies using freshly resected human tissue were performed as described previously (Gundersen et al., 2016; Ruffell et al., 2012).

Statistics

Kruskal-Wallis tests were used to determine statistically significant differences in unpaired and paired data. The Spearman correlation coefficient was used to assess correlations of cell percentages and densities among cell lineages. Overall survival was estimated using Kaplan-Meier methods, and differences were assessed with log-rank tests. An unsupervised hierarchical clustering was performed with Ward's minimum variance method (hclust from R). The p values were adjusted for multiple comparisons using Benjamini-Hochberg false discovery rate (FDR) adjustments. All statistical calculations were performed by R v.3.2.3 software (<http://www.r-project.org>) and SAS v.9.4 software. p < 0.05 was considered statistically significant.

Study Approval

All studies involving human tissue were approved by institutional review board (IRB) (protocol 809 and 3609), and written informed consent was obtained.

ACCESSION NUMBERS

The accession number for the flow cytometry data reported in this paper is Flow Repository: FR-FCM-ZY3A.

SUPPLEMENTAL INFORMATION

Supplemental Information includes Supplemental Experimental Procedures, eight figures, and three tables and can be found with this article online at <http://dx.doi.org/10.1016/j.celrep.2017.03.037>.

AUTHOR CONTRIBUTIONS

T.T., S.K., and L.M.C. conceived and designed the experiments; T.T. wrote the manuscript, which was edited by L.M.C.; J.W.G. reviewed the manuscript and consulted on computational algorithms and software; T.T., R.K., and G.C. performed the experiments; T.T., R.N.B., V.A., G.T., Y.H.C., A.B., P.L., and A.A.M. developed computational algorithms and software; E.R.L., L.Z., and E.M.J. contributed to design of IHC panels and provided tissues for PDAC studies; M.M. supported statistical data analysis; D.S., M.F.K.-M., E.E.R., D.R.C., and P.W.F. provided tissues for human HNSCC analyses; and L.M.C. supervised the project.

ACKNOWLEDGMENTS

The authors thank Justin Tibbitts, Teresa Beechwood, and Chase Smith for regulatory and technical assistance and Dr. Gunderson for FACS analysis. This project was supported by the Oregon Clinical and Translational Research Institute (OCTRI, UL1TR000128), the National Center for Advancing Translational Sciences (NCATS) at the NIH, a Stand Up To Cancer-Lustgarten Foundation Pancreatic Cancer Convergence Dream Team Translational Research Grant (L.M.C., A.A.M., and E.M.J.), and the OHSU Knight Cancer Institute (P30 CA069533-17). M.F.K.-M. acknowledges support from the NCI (CA192405). L.M.C. acknowledges support from the NIH/NCI, DOD BCRP Era of Hope Scholar Expansion Award, Breast Cancer Research Foundation, Susan B. Komen Foundation, and Brenden-Colson Center for Pancreatic Health. A patent application related to the methodology described in the present work has been filed by T.T., S.K., R.N.B., V.A., and L.M.C.

Received: December 6, 2016

Revised: February 4, 2017

Accepted: March 10, 2017

Published: April 4, 2017

REFERENCES

- Affara, N.I., Ruffell, B., Medler, T.R., Gunderson, A.J., Johansson, M., Bornstein, S., Bergsland, E., Steinhoff, M., Li, Y., Gong, Q., et al. (2014). B cells regulate macrophage phenotype and response to chemotherapy in squamous carcinomas. *Cancer Cell* 25, 809–821.
- Carpenter, A.E., Jones, T.R., Lamprecht, M.R., Clarke, C., Kang, I.H., Friman, O., Guertin, D.A., Chang, J.H., Lindquist, R.A., Moffat, J., et al. (2006). CellProfiler: image analysis software for identifying and quantifying cell phenotypes. *Genome Biol.* 7, R100.
- DeNardo, D.G., Brennan, D.J., Rexhepaj, E., Ruffell, B., Shiao, S.L., Madden, S.F., Gallagher, W.M., Wadhvani, N., Keil, S.D., Junaid, S.A., et al. (2011). Leukocyte complexity predicts breast cancer survival and functionally regulates response to chemotherapy. *Cancer Discov.* 1, 54–67.
- Fridman, W.H., Pagès, F., Sautès-Fridman, C., and Galon, J. (2012). The immune contexture in human tumours: impact on clinical outcome. *Nat. Rev. Cancer* 12, 298–306.
- Galon, J., Costes, A., Sanchez-Cabo, F., Kirilovsky, A., Mlecnik, B., Lagorce-Pagès, C., Tosolini, M., Camus, M., Berger, A., Wind, P., et al. (2006). Type, density, and location of immune cells within human colorectal tumors predict clinical outcome. *Science* 313, 1960–1964.
- Gentles, A.J., Newman, A.M., Liu, C.L., Bratman, S.V., Feng, W., Kim, D., Nair, V.S., Xu, Y., Khuong, A., Hoang, C.D., et al. (2015). The prognostic landscape of genes and infiltrating immune cells across human cancers. *Nat. Med.* 21, 938–945.
- Glass, G., Papin, J.A., and Mandell, J.W. (2009). SIMPLE: a sequential immunoperoxidase labeling and erasing method. *J. Histochem. Cytochem.* 57, 899–905.
- Gunderson, A.J., Kaneda, M.M., Tsujikawa, T., Nguyen, A.V., Affara, N.I., Ruffell, B., Gorjestani, S., Liudahl, S.M., Truitt, M., Olson, P., et al. (2016). Bruton's tyrosine kinase-dependent immune cell cross-talk drives pancreas cancer. *Cancer Discov.* 6, 270–285.
- Keck, M.K., Zuo, Z., Khattri, A., Stricker, T.P., Brown, C., Imanguli, M., Rieke, D., Endhardt, K., Fang, P., Brägelmann, J., et al. (2014). Integrative analysis of head and neck cancer identifies two biologically distinct HPV and three non-HPV subtypes. *Clin. Cancer Res.* 21, 870–881.
- Lan, H.Y., Mu, W., Nikolic-Paterson, D.J., and Atkins, R.C. (1995). A novel, simple, reliable, and sensitive method for multiple immunoenzyme staining: use of microwave oven heating to block antibody crossreactivity and retrieve antigens. *J. Histochem. Cytochem.* 43, 97–102.
- Liu, Y., Wang, Z., De La Torre, R., Barling, A., Tsujikawa, T., Hornick, N., Hanifin, J., Simpson, E., Wang, Y., Swanzey, E., et al. (2017). Trim32 deficiency enhances Th2 immunity and predisposes to features of atopic dermatitis. *J. Invest. Dermatol.* 137, 359–366.
- Lutz, E.R., Wu, A.A., Bigelow, E., Sharma, R., Mo, G., Soares, K., Solt, S., Dorman, A., Wamwea, A., Yager, A., et al. (2014). Immunotherapy converts non-immunogenic pancreatic tumors into immunogenic foci of immune regulation. *Cancer Immunol. Res.* 2, 616–631.
- Lyford-Pike, S., Peng, S., Young, G.D., Taube, J.M., Westra, W.H., Akpeng, B., Bruno, T.C., Richmon, J.D., Wang, H., Bishop, J.A., et al. (2013). Evidence for a role of the PD-1:PD-L1 pathway in immune resistance of HPV-associated head and neck squamous cell carcinoma. *Cancer Res.* 73, 1733–1741.
- Mantovani, A., Sozzani, S., Locati, M., Allavena, P., and Sica, A. (2002). Macrophage polarization: tumor-associated macrophages as a paradigm for polarized M2 mononuclear phagocytes. *Trends Immunol.* 23, 549–555.
- Padmanabhan, K., Eddy, W.F., and Crowley, J.C. (2010). A novel algorithm for optimal image thresholding of biological data. *J. Neurosci. Methods* 193, 380–384.
- Paley, M.A., Kroy, D.C., Odorizzi, P.M., Johnnidis, J.B., Dolfi, D.V., Barnett, B.E., Bikoff, E.K., Robertson, E.J., Lauer, G.M., Reiner, S.L., and Wherry, E.J. (2012). Progenitor and terminal subsets of CD8+ T cells cooperate to contain chronic viral infection. *Science* 338, 1220–1225.
- Palucka, A.K., and Coussens, L.M. (2016). The basis of oncoimmunology. *Cell* 164, 1233–1247.
- Pardoll, D.M. (2012). The blockade of immune checkpoints in cancer immunotherapy. *Nat. Rev. Cancer* 12, 252–264.
- Parsa, A.T., Waldron, J.S., Panner, A., Crane, C.A., Parney, I.F., Barry, J.J., Cachola, K.E., Murray, J.C., Tihan, T., Jensen, M.C., et al. (2007). Loss of tumor suppressor PTEN function increases B7-H1 expression and immunoresistance in glioma. *Nat. Med.* 13, 84–88.
- Patel, S.P., and Kurzrock, R. (2015). PD-L1 expression as a predictive biomarker in cancer immunotherapy. *Mol. Cancer Ther.* 14, 847–856.
- Ruffell, B., and Coussens, L.M. (2015). Macrophages and therapeutic resistance in cancer. *Cancer Cell* 27, 462–472.
- Ruffell, B., DeNardo, D.G., Affara, N.I., and Coussens, L.M. (2010). Lymphocytes in cancer development: polarization towards pro-tumor immunity. *Cytokine Growth Factor Rev.* 21, 3–10.
- Ruffell, B., Au, A., Rugo, H.S., Esserman, L.J., Hwang, E.S., and Coussens, L.M. (2012). Leukocyte composition of human breast cancer. *Proc. Natl. Acad. Sci. USA* 109, 2796–2801.
- Ruffell, B., Chang-Strachan, D., Chan, V., Rosenbusch, A., Ho, C.M., Pryer, N., Daniel, D., Hwang, E.S., Rugo, H.S., and Coussens, L.M. (2014). Macrophage IL-10 blocks CD8+ T cell-dependent responses to chemotherapy by suppressing IL-12 expression in intratumoral dendritic cells. *Cancer Cell* 26, 623–637.
- Ruifrok, A.C., Katz, R.L., and Johnston, D.A. (2003). Comparison of quantification of histochemical staining by hue-saturation-intensity (HSI) transformation and color-deconvolution. *Appl. Immunohistochem. Mol. Morphol.* 11, 85–91.
- Schneider, C.A., Rasband, W.S., and Eliceiri, K.W. (2012). NIH Image to ImageJ: 25 years of image analysis. *Nat. Methods* 9, 671–675.
- Soares, K.C., Rucki, A.A., Wu, A.A., Olino, K., Xiao, Q., Chai, Y., Wamwea, A., Bigelow, E., Lutz, E., Liu, L., et al. (2015). PD-1/PD-L1 blockade together with vaccine therapy facilitates effector T-cell infiltration into pancreatic tumors. *J. Immunother.* 38, 1–11.
- Thurlow, J.K., Peña Murillo, C.L., Hunter, K.D., Buffa, F.M., Patiar, S., Betts, G., West, C.M., Harris, A.L., Parkinson, E.K., Harrison, P.R., et al. (2010). Spectral clustering of microarray data elucidates the roles of microenvironment remodeling and immune responses in survival of head and neck squamous cell carcinoma. *J. Clin. Oncol.* 28, 2881–2888.
- Topalian, S.L., Drake, C.G., and Pardoll, D.M. (2012). Targeting the PD-1/B7-H1 (PD-L1) pathway to activate anti-tumor immunity. *Curr. Opin. Immunol.* 24, 207–212.
- Tramu, G., Pillez, A., and Leonardelli, J. (1978). An efficient method of antibody elution for the successive or simultaneous localization of two antigens by immunocytochemistry. *J. Histochem. Cytochem.* 26, 322–324.

Twyman-Saint Victor, C., Rech, A.J., Maity, A., Rengan, R., Pauken, K.E., Stelekati, E., Benci, J.L., Xu, B., Dada, H., Odorizzi, P.M., et al. (2015). Radiation and dual checkpoint blockade activate non-redundant immune mechanisms in cancer. *Nature* *520*, 373–377.

Wählby, C., Sintorn, I.M., Erlandsson, F., Borgefors, G., and Bengtsson, E. (2004). Combining intensity, edge and shape information for 2D and 3D segmentation of cell nuclei in tissue sections. *J. Microsc.* *215*, 67–76.

Wherry, E.J., and Kurachi, M. (2015). Molecular and cellular insights into T cell exhaustion. *Nat. Rev. Immunol.* *15*, 486–499.

Zhang, L., Conejo-Garcia, J.R., Katsaros, D., Gimotty, P.A., Massobrio, M., Regnani, G., Makrigiannakis, A., Gray, H., Schlienger, K., Liebman, M.N., et al. (2003). Intratumoral T cells, recurrence, and survival in epithelial ovarian cancer. *N. Engl. J. Med.* *348*, 203–213.

Cell Reports, Volume 19

Supplemental Information

Quantitative Multiplex Immunohistochemistry

Reveals Myeloid-Inflamed Tumor-Immune

Complexity Associated with Poor Prognosis

Takahiro Tsujikawa, Sushil Kumar, Rohan N. Borkar, Vahid Azimi, Guillaume Thibault, Young Hwan Chang, Ariel Balter, Rie Kawashima, Gina Choe, David Sauer, Edward El Rassi, Daniel R. Clayburgh, Molly F. Kulesz-Martin, Eric R. Lutz, Lei Zheng, Elizabeth M. Jaffee, Patrick Leyshock, Adam A. Margolin, Motomi Mori, Joe W. Gray, Paul W. Flint, and Lisa M. Coussens

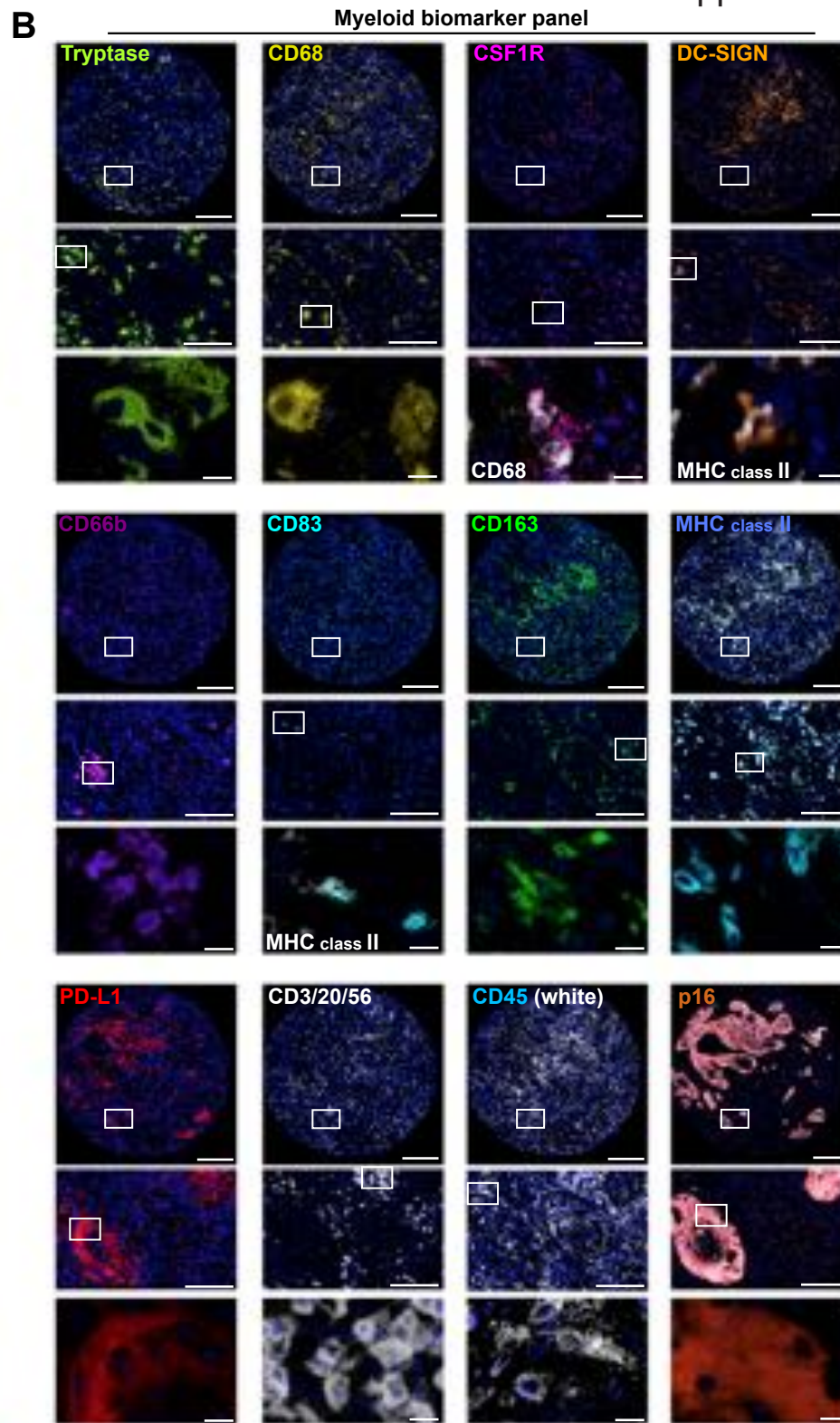
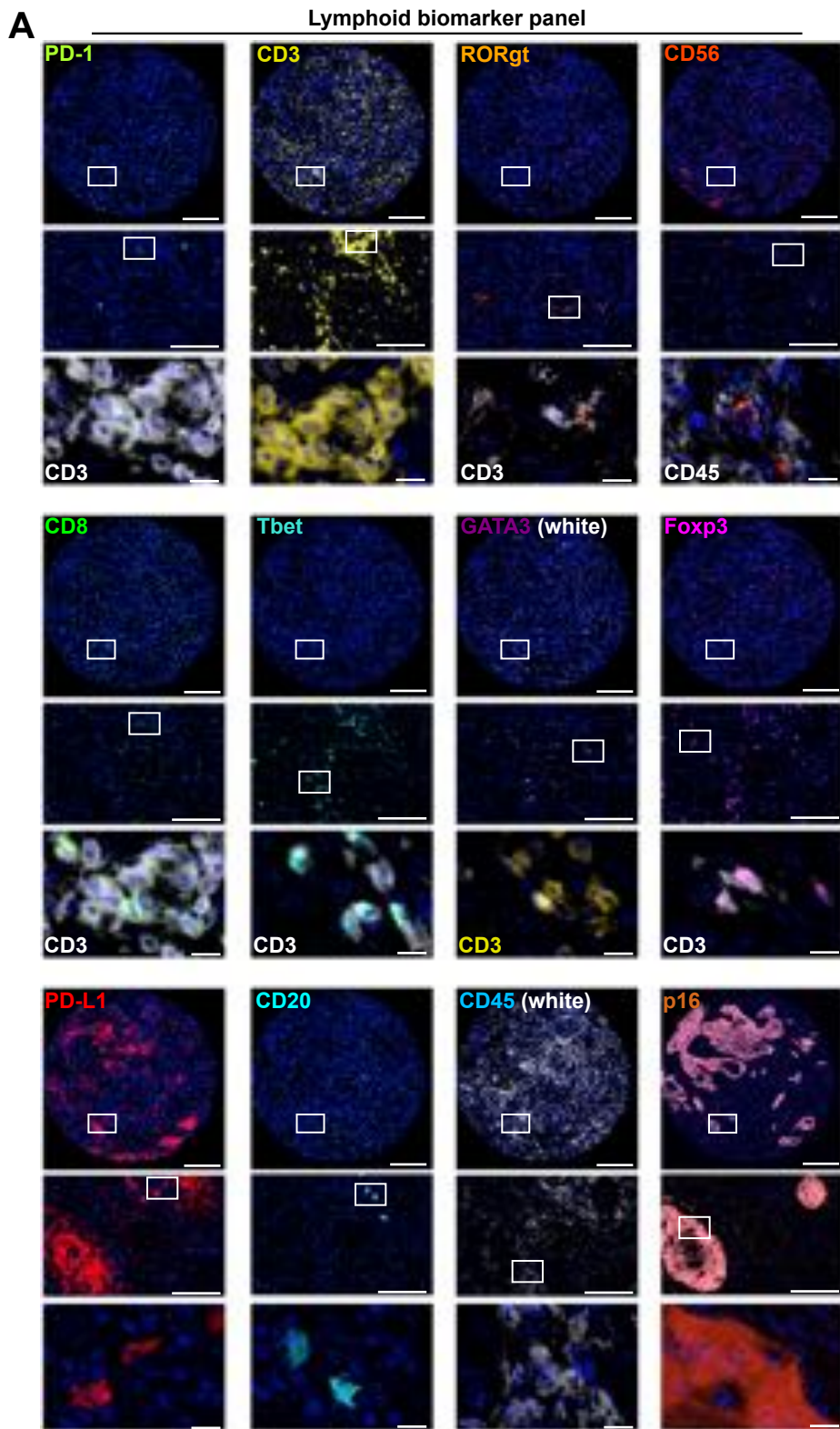


Figure S1 in reference to Figure 1: Pseudo-colored single marker IHC images from sequential multiplex IHC. Single channel images representing the lymphoid (**Figure 1E**) and myeloid (**Figure 1F**) biomarker antibody panels are shown in (**A**) and (**B**), respectively. Boxes represent area magnified. When indicated, CD3, CD68, and MHC class II images are merged to show colocalization in bottom panels. Scale bars = 500 μm (top) and 100 μm (middle), and 10 μm (bottom).

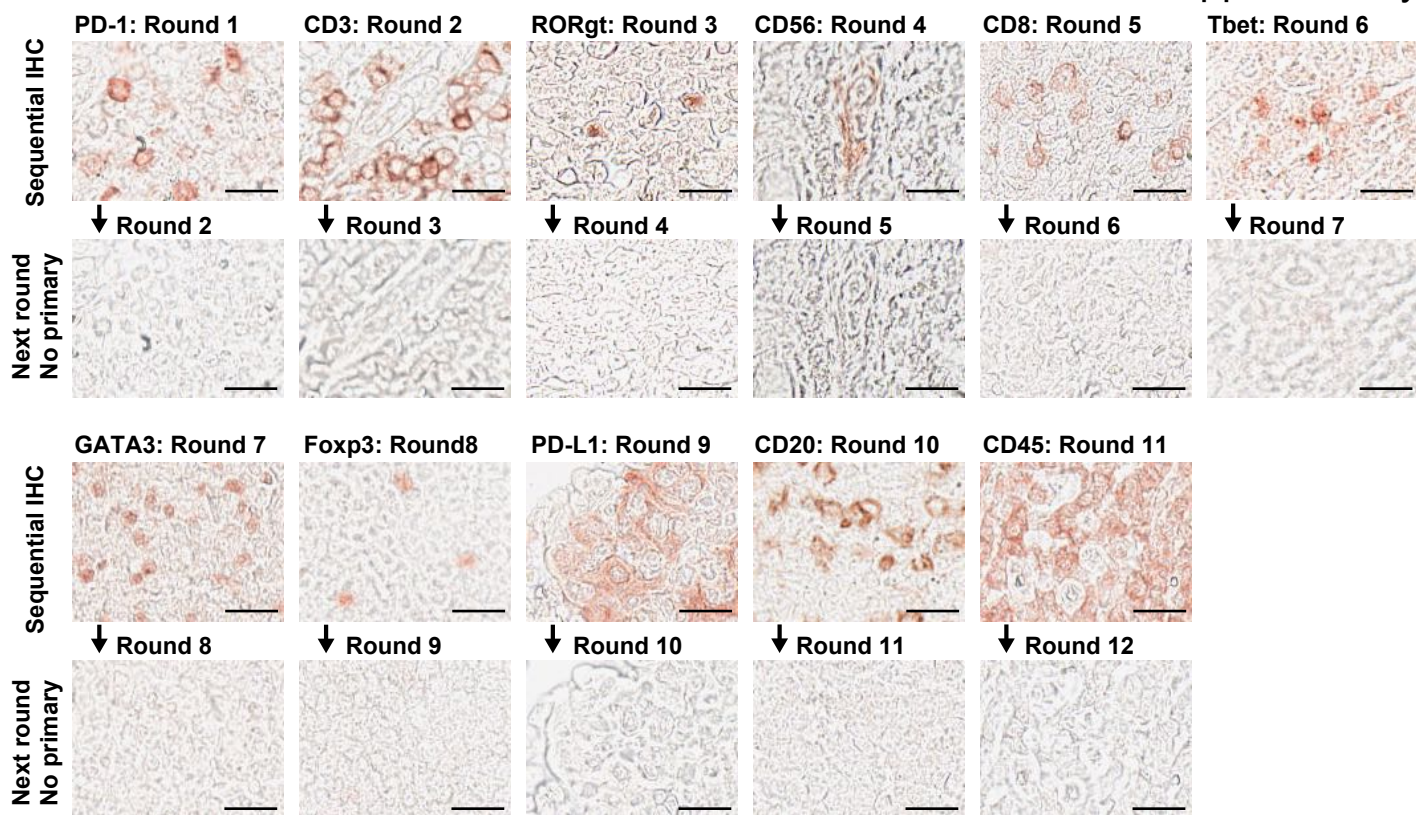
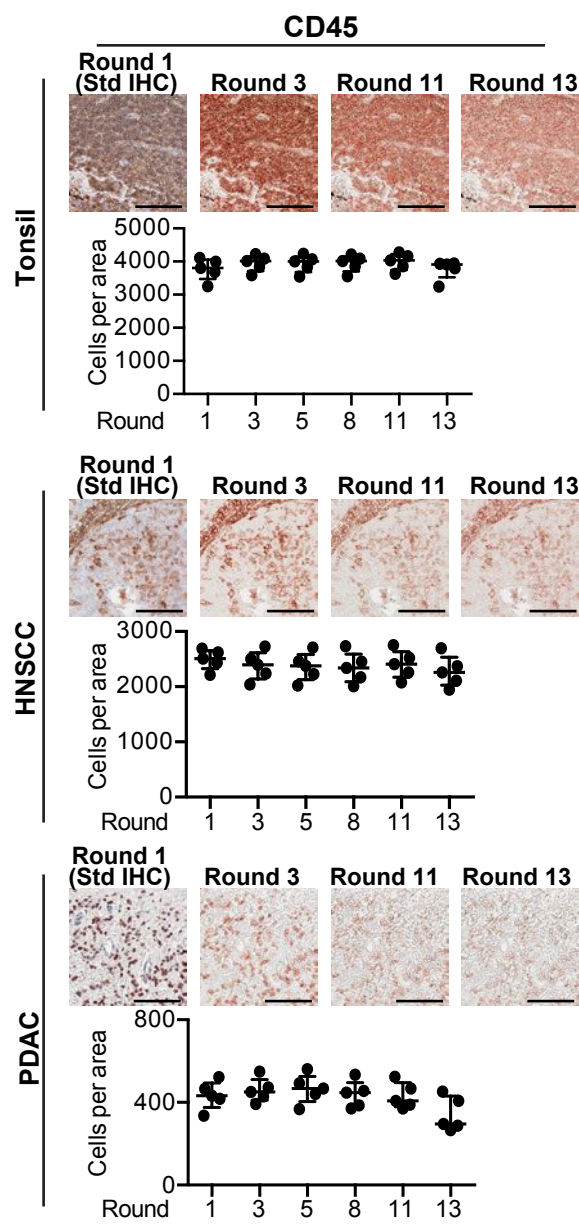
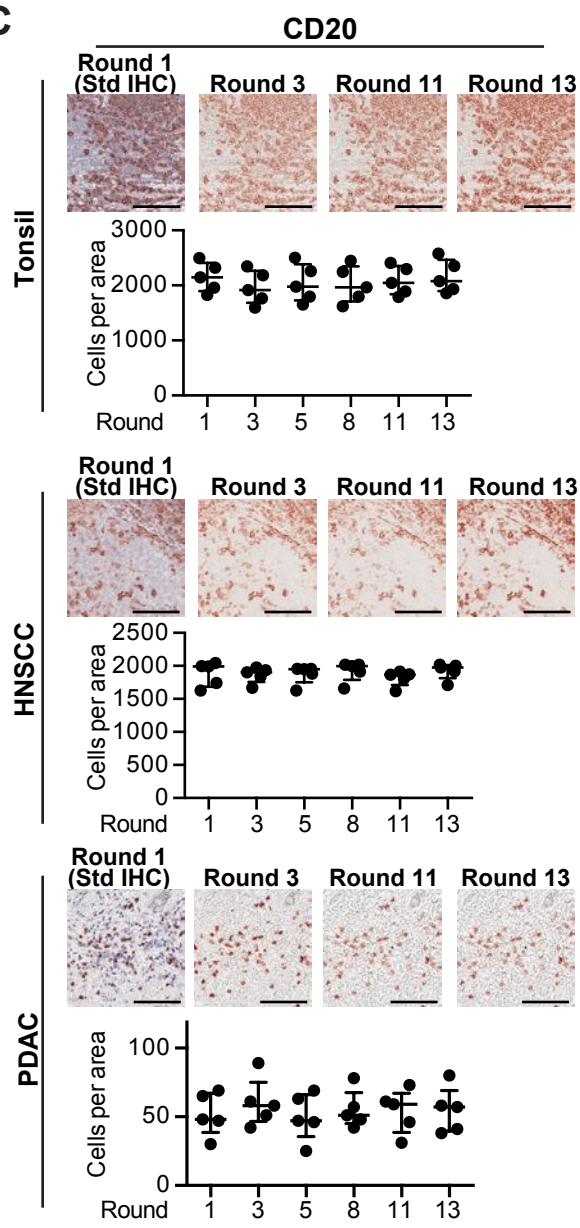
A**B****C**

Figure S2 in reference to Figure 1: Validation of chromogenic multiplex IHC. (A) To validate antibody-stripping protocol, staining was performed in the same number of rounds in corresponding to the protocol shown in **Table S1**. Images represent chromogenic staining with labeled biomarkers and the number of round (top panel). Following AEC wash and antibody stripping, complete removal of antibody and signal was confirmed by incubating with only the detection reagent and AEC in the next sequential round (bottom panel). Scale bars = 10 μm . (B, C) Comparison between standard IHC and multiple rounds of sequential IHC was performed in detection of CD45 (B) and CD20 (C) in human tonsil, head and neck squamous cell carcinoma (HNSCC), and pancreatic ductal adenocarcinoma (PDAC) tissue. Top panel images represent findings of standard IHC (round 1) and AEC images in IHC round 3, 11, and 13. Scale bars = 100 μm . Bottom graphs show cell counts of CD45⁺ (B) or CD20⁺ (C) cells quantified in five regions of 62500 μm^2 area by image cytometry. No significant reduction of detection was observed when comparing IHC round 1 to 13. The bars show mean \pm SD. Statistical significance determined by Kruskal-Wallis test.

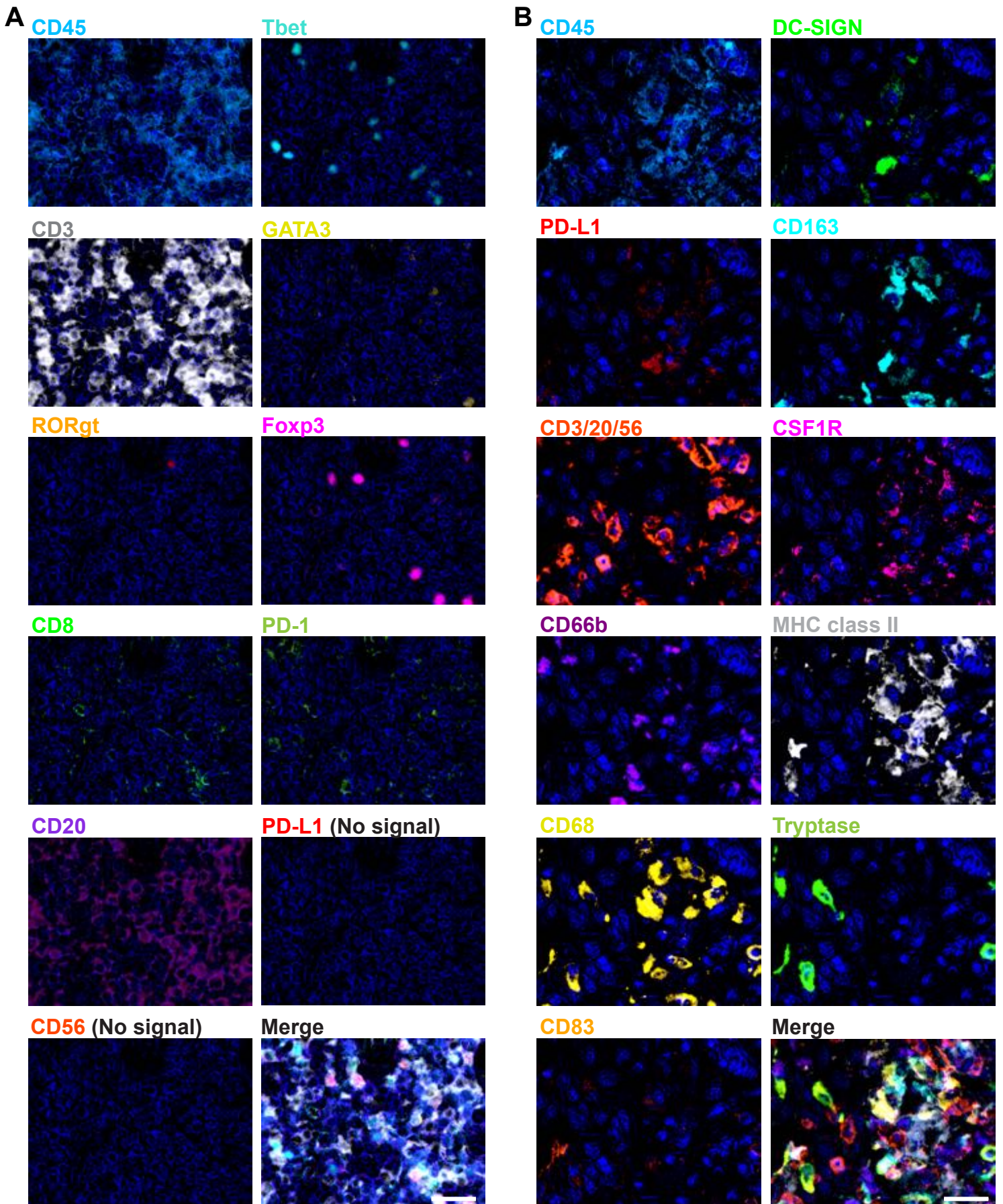


Figure S3 in reference to Figure 2: Pseudo-colored images of single-stained multi-plexmultiplex cycles shown in Figure 2. Single channel images in support of **Figures 2A and 2B** are shown in (A) and (B), respectively. Scale bars = 50 μm .

Figure S4 in reference to Figure 3: Validation of image cytometry analysis. (A) Image cytometry analysis enables visualization of positional linkage between dot plots and original images. Colored dots in the left panels are pointed out in the original AEC images (middle panel), and multiplexed IHC images (right panels). Scale bars = 100 μm . Right panel shows image cytometry findings on negative control slides. (B, C) Density plots in negative control slides are shown in support of **Figures 3C and D**. The x and y axes are shown on a logarithmic scale. (D) Comparison between image cytometry and flow cytometry in human PDAC tissues (N = 8). Representative density plots from flow cytometry (upper) and image cytometry (lower) are shown. (E) Pairwise associations of T cell ($\text{CD45}^+ \text{CD3}^+$), B cell ($\text{CD45}^+ \text{CD19}^+$ or CD20^+), CD8^+ T cell ($\text{CD45}^+ \text{CD3}^+ \text{CD8}^+$) of total CD45^+ cells are assessed by Spearman correlation coefficient. Estimated regression lines for each category were shown.

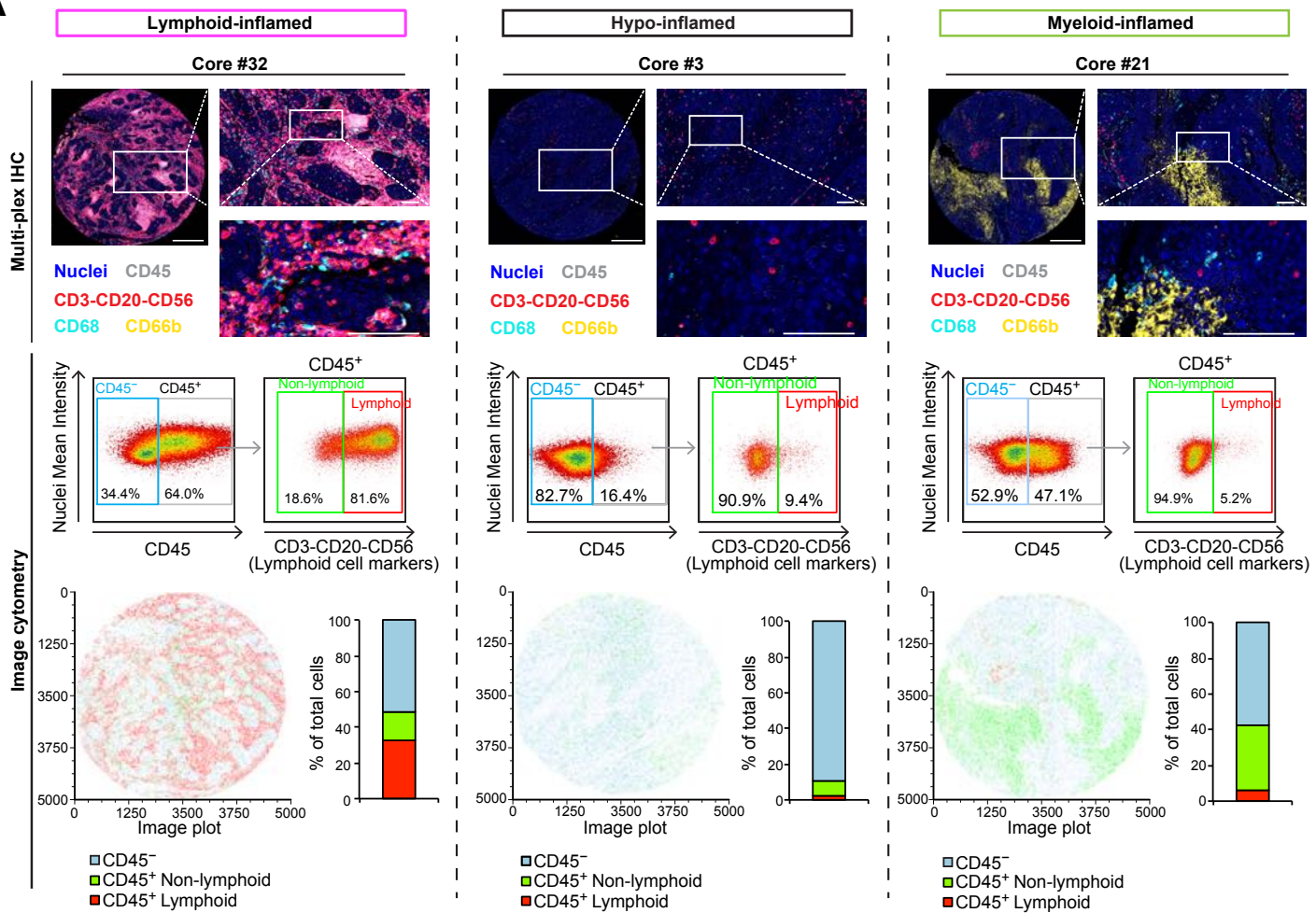
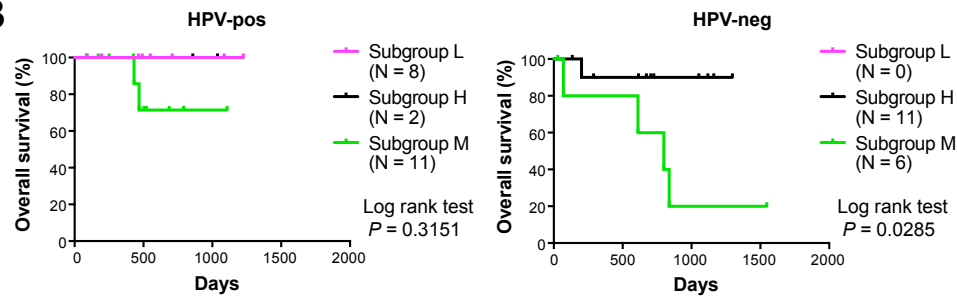
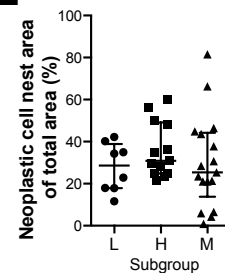
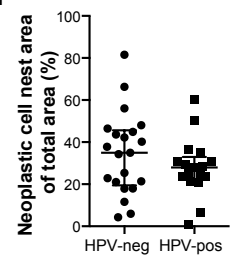
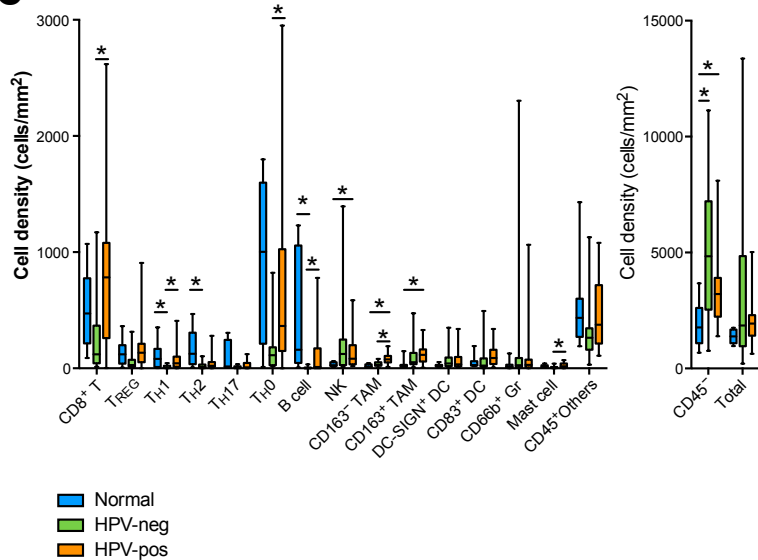
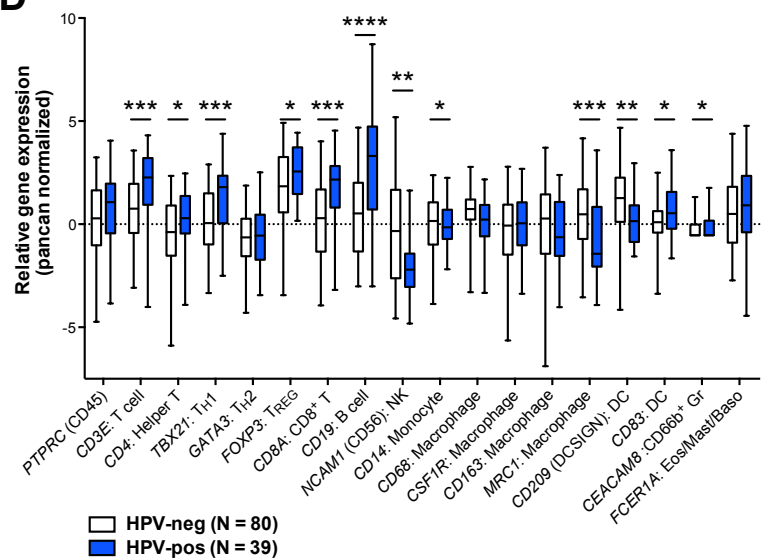
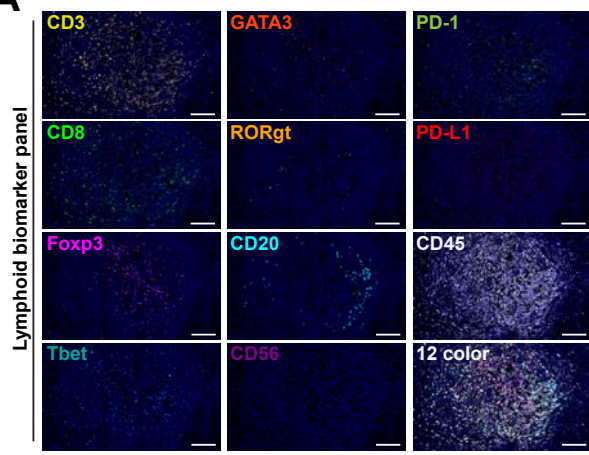
A**B****E****F****C****D**

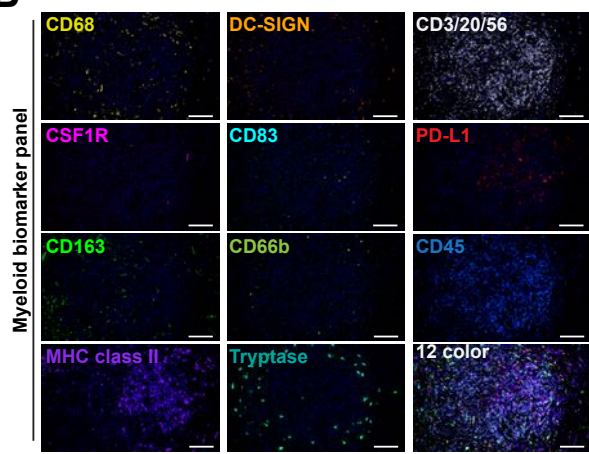
Figure S5 in reference to Figure 4: Cell density, composition, and TCGA analysis for subclassification of HNSCC.

(A) Micrographs show multiplex IHC findings in lymphoid-, hypo-, and myeloid-inflamed subgroups in HNSCC (**Figure 4C**), showing high infiltration of lymphoid cell populations in core #32, hypo-infiltration of CD45⁺ leukocytes in core #3, and high infiltration of CD68⁺ and CD66b⁺ cells in core #21. Boxes and hashed lines represent area magnified. Biomarkers and color annotations were shown in bottom left. Scale bars = 500 μm (top left) and 100 μm (top right and bottom right). Image cytometry-based quantification was shown in corresponding to IHC images. Top two panels show density plots of CD45 and cocktail antibodies of CD3, CD20 and CD56 (lymphoid cell markers). Image plots (bottom left) depict location of cells identified above by image cytometry, according to color markers below. Composition graphs (bottom right) show quantified cell percentages of CD45⁻, CD45⁺CD3-CD20-CD56⁻ (non-lymphoid) and CD45⁺CD3-CD20-CD56⁺ (lymphoid) cells of total cells, according to color markers below. (B) Kaplan-Meier analyses of overall survival of HPV-positive and negative HNSCC patients were shown with stratification by lymphoid- (L), hypo- (H) and myeloid- (M) inflamed subgroups. Statistical significance was determined via log-rank test. (C) The box-whisker plots of cell density in support of **Figure 4C** are shown. *, **, and *** show $P < 0.05$, 0.01, and 0.001, respectively, by Kruskal-Wallis tests with FDR adjustments. Bars, boxes and whiskers represent median, interquartile range and range, respectively. (D) Comparison of gene expression between HPV-positive and HPV-negative HNSCC from The Cancer Genome Atlas (N = 39 and 80, respectively). TCGA HNSCC mRNA gene expression by pancan-normalized RNAseq (Illumina-HiSeq) (N = 564) were downloaded from UCSC cancer browser at <https://genome-cancer.ucsc.edu> (Data obtained in October, 2014). 434 samples without available information of HPV-status were excluded, and total of 119 cases were analyzed by expression of immune cell lineage markers. Vertical axis shows log₂-based gene expression normalized to all TCGA cancer types. Bars, boxes and whiskers represent median, interquartile range and range, respectively. *, **, ***, and **** show $P < 0.05$, 0.01, 0.001, and 0.0001, respectively, by Kruskal-Wallis tests with FDR adjustments. (E, F) Area of neoplastic cell nest (% of total tissue area) was immunohistochemically assessed based on p16 (HPV-positive) and EpCAM (HPV-negative), and compared among the three subgroups indicated in **Figure 4C** (D) or between groups stratified by HPV-status (E). Each single dot represents one core/individual in TMA. Statistical significance in (D) and (E) was determined by Kruskal-Wallis test, and p values in (D) were adjusted by FDR.

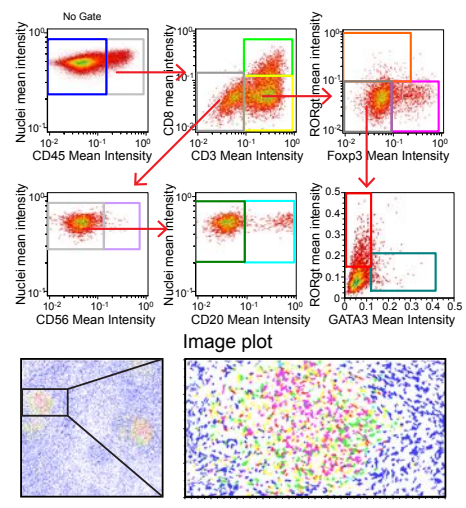
A



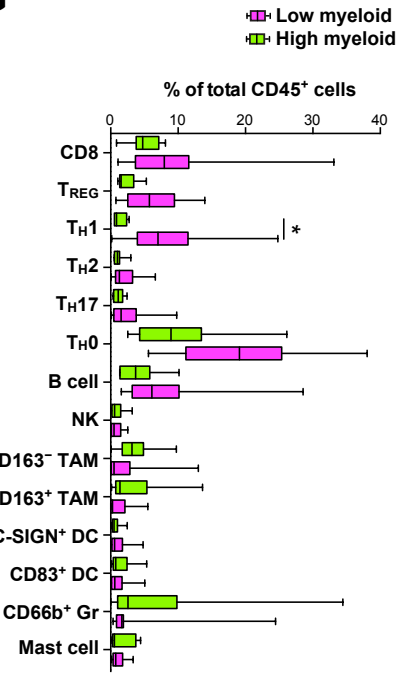
B



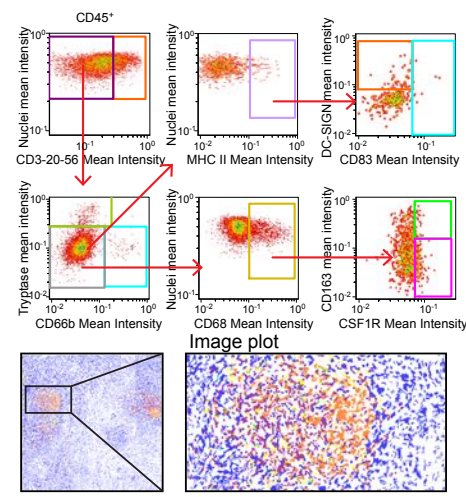
C



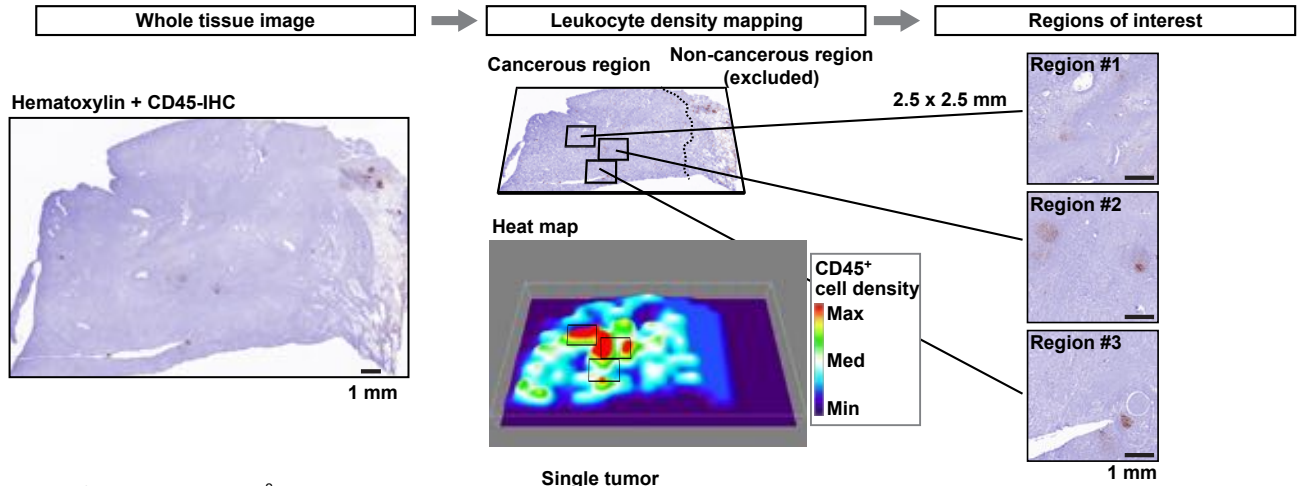
G



D



E



F

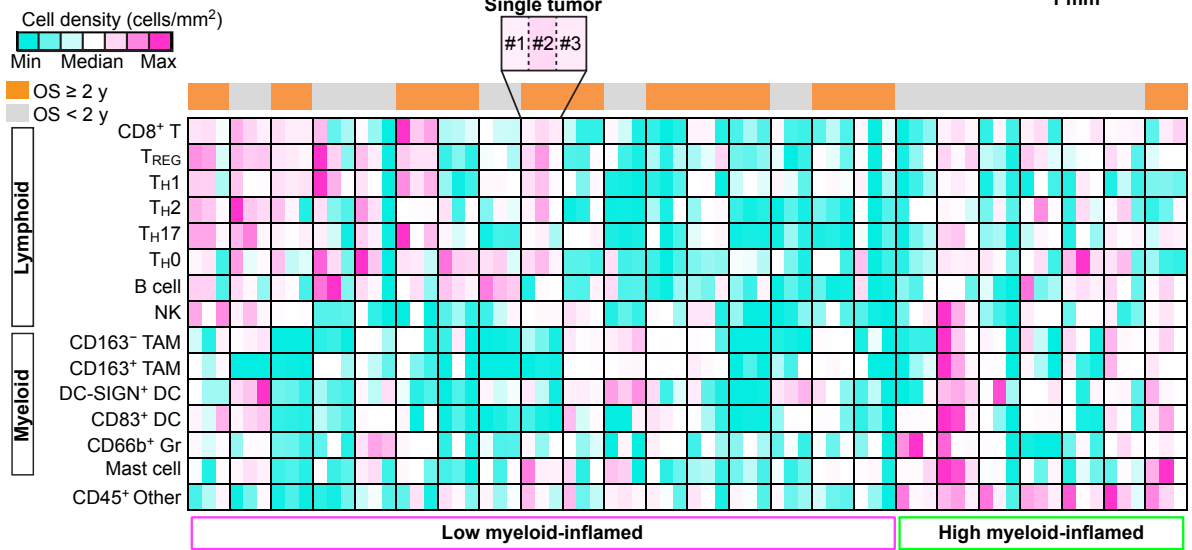
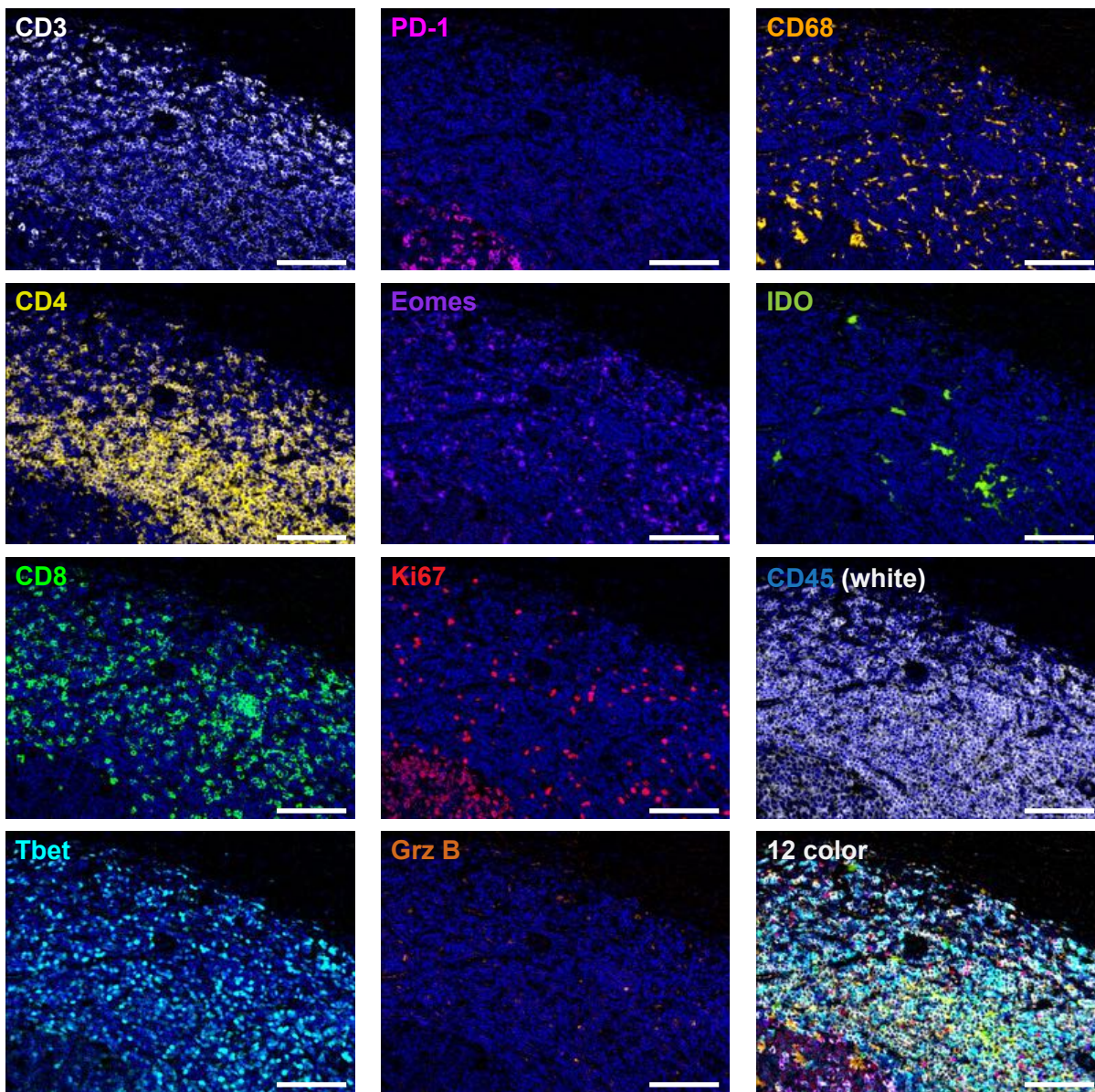
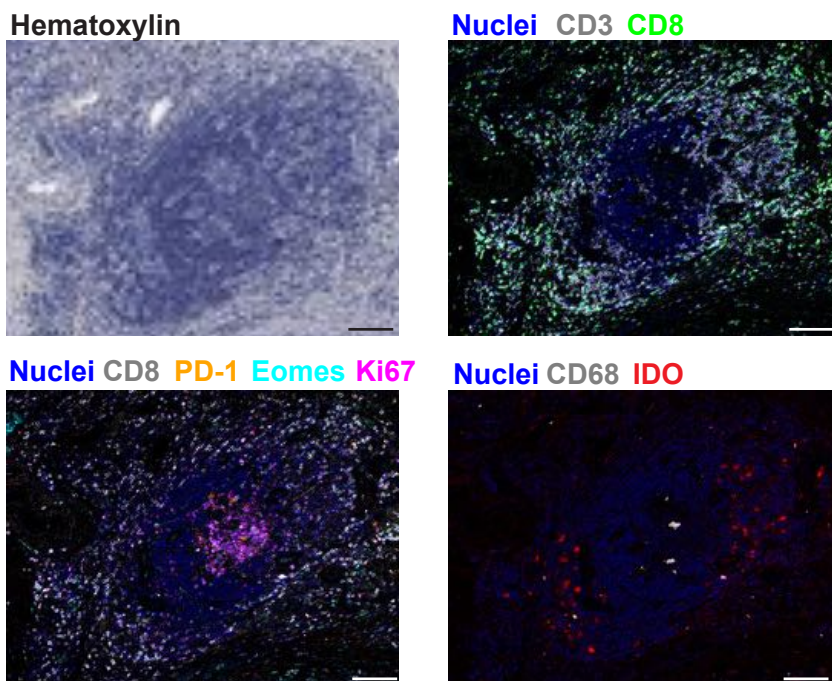


Figure S6 in reference to Figure 5: Region of interest (ROI) selection based on leukocyte hot spot analysis in neoadjuvant GVAX treated PDAC. (A, B) Pseudo-colored images of single-stained multiplex cycles shown in **Figure 5A and 5B** are shown in (A) and (B), respectively. Scale bars = 100 μm . (C, D) Image cytometry analyses for lymphoid (C) and myeloid (D) biomarker panels based on **Figure 5A** images are shown, together with corresponding image plots visualizing cells identified in the gating strategies. (E) Overview of mapping analyses of CD45⁺ leukocyte cell densities. Following generation of whole tissue-based pseudo-IHC images from hematoxylin and CD45-IHC image (left panel), a heat map of leukocyte cell density is generated based on quantification of CD45⁺ cells per area (middle panels). Excluding pathologist-evaluated non-malignant regions, three highest leukocyte density regions are selected and exported as ROIs for downstream image analysis (right panels). Magnification is shown. (F) Each single cell in the heat map of **Figure 5B** is split to three columns from independent ROIs. The data is visualized in a new heat map according to color scale (upper left), showing that three different ROIs are basically sharing similar signatures across immune cell lineages with mild variation. Overall survival (OS) and low/high myeloid inflamed profiles defined in **Figure 5B** are shown. (G) Immune cell percentages comparing low and high myeloid-inflamed profiles were quantified as a percentage of total CD45⁺ cells. Statistical significance was determined via Kruskal-Wallis tests with FDR adjustments, with * $P < 0.05$.

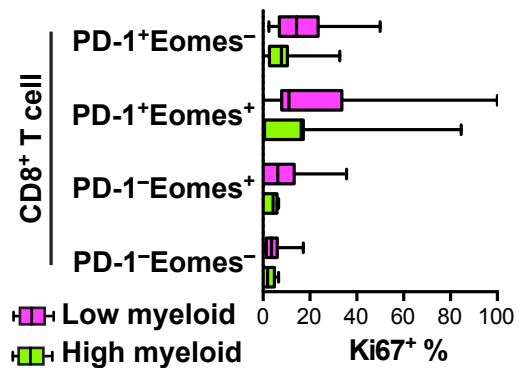
A



B



C



D

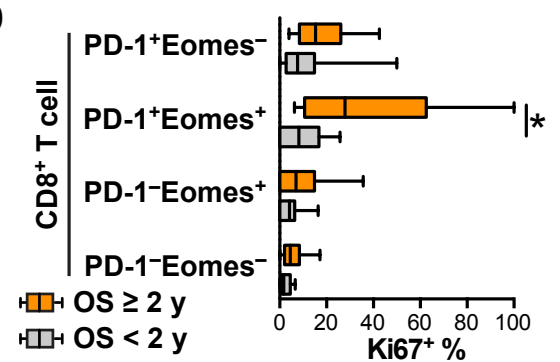
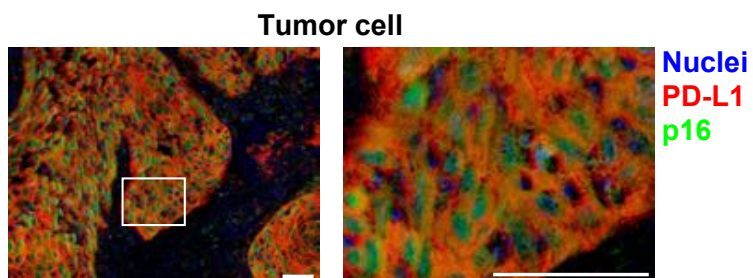
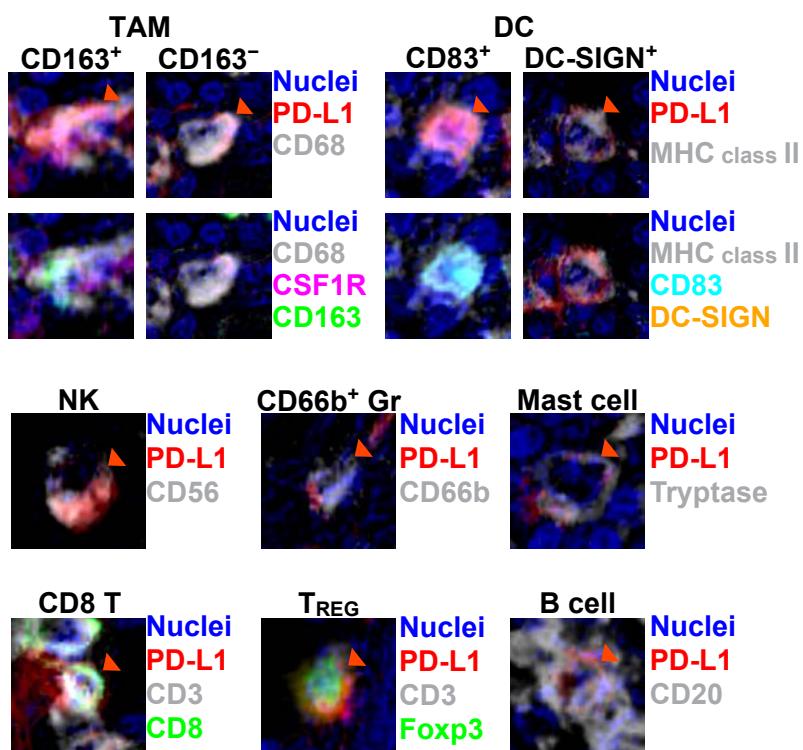


Figure S7 in reference to Figure 6: T cell functional biomarker panel images and quantification. (A) Single channel images of T cell functional biomarker panels in support of **Figure 6A** are shown. (B) In support of **Figure 6B**, hematoxylin and multiplex IHC images are shown in a lymphoid aggregative area of human PDAC tissues. Biomarkers and color annotations were shown. Scale bars = 100 μm . (C, D) Box whisker plots show Ki67 positive percentages evaluated in each CD8⁺ T cell subpopulation, comparing low vs high myeloid-inflamed profiles and long and short overall survival (OS) groups. Bars, boxes and whiskers represent median, interquartile range and range, respectively. Statistical significances between the two groups were determined via Kruskal-Wallis tests with FDR adjustments, with * $P < 0.05$.

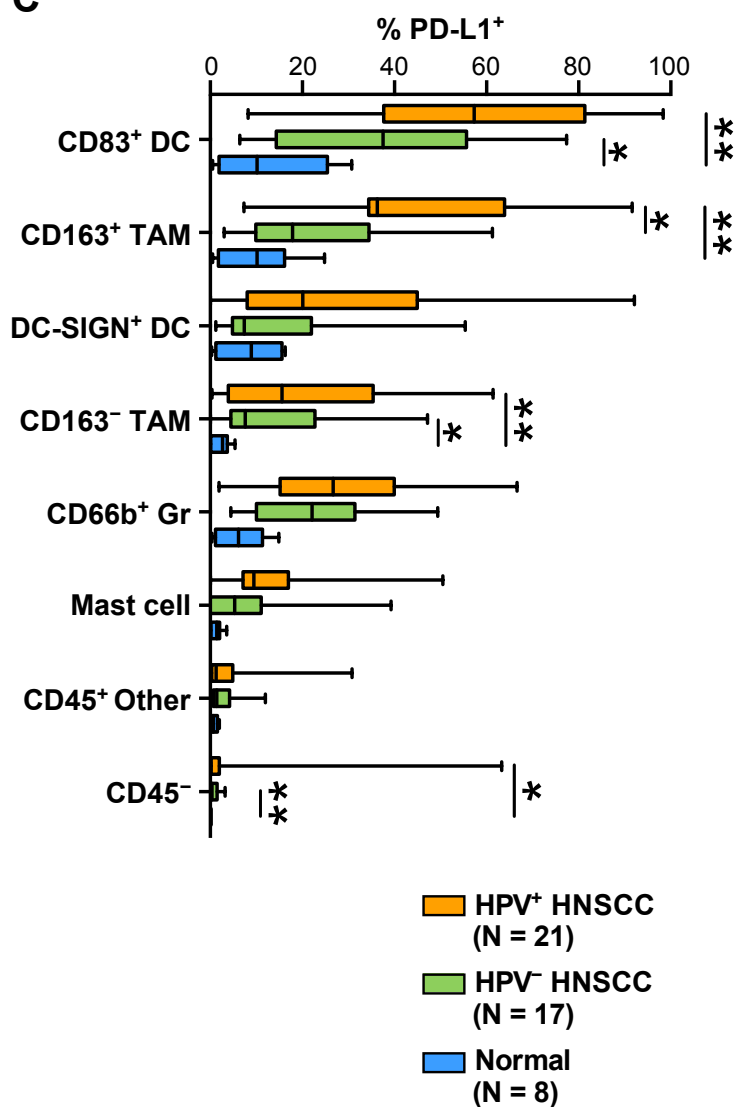
A



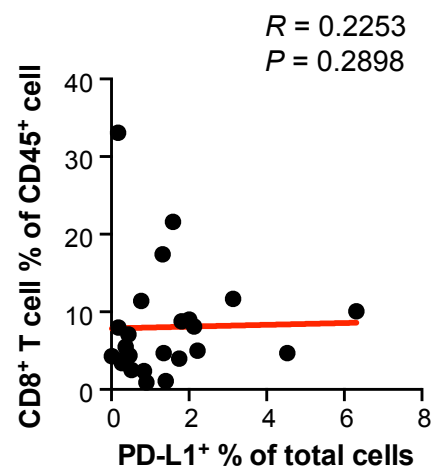
B



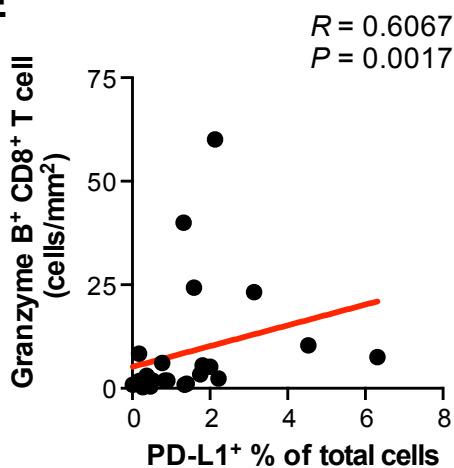
C



D



E



F

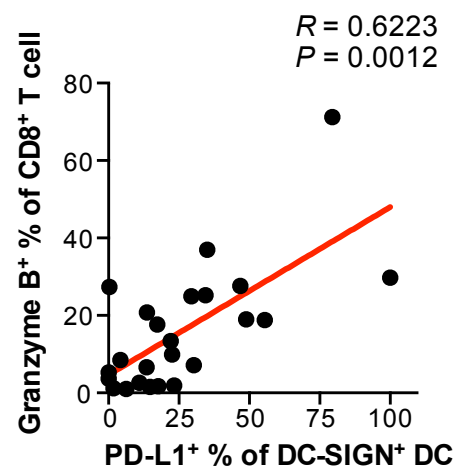


Figure S8 in reference to Figure 7: PD-L1 expression profiles in neoplastic and immune cell lineages. (A) PD-L1 expression on neoplastic cells in HPV-positive HNSCC tissue. Box denotes area magnified in right. Scale bars = 50 μm . (B) Micrographs showing PD-L1⁺ immune cells (red arrowheads) in 20 μm square frames. (C) PD-L1-positive % in each cell lineage was quantified by image cytometry. Bars, boxes and whiskers represent median, interquartile range and range, respectively. * $P < 0.05$, and ** $P < 0.01$, by Kruskal-Wallis tests with FDR adjustments. (D, E) Spearman correlations of granzyme B⁺ CD8⁺ T cells of CD45⁺ cells (D) or Granzyme B⁺ CD8⁺ T cell density (E) versus PD-L1⁺ percentages of total cells were shown with estimated regression lines (red) in the neoadjuvant GVAX-treated PDAC cohort (N = 24). (F) Spearman correlation of PD-L1⁺% of DC-SIGN⁺ DCs and Granzyme B⁺% of CD8⁺ T cells was shown with estimated regression lines (N = 24).

Table S1 in reference to Figure 1. Sequential IHC panel information.

Lymphoid biomarker panel

		Round 1	Round 2	Round 3	Round 4	Round 5	Round 6
Primary Ab	Hematoxylin	PD-1	CD3	RORgt	CD56	CD8	T-bet
Supplier	Dako	Abcam	Thermo Scientific	EMD Millipore	Santa Cruz Biotech	Thermo Scientific	Santa Cruz Biotech
Clone/Product#	S3301	NAT105	SP7	6F3.1	123C3	C8/144B	H-210
Concentration		1:50	1:150	1:200	1:25	1:100	1:100
Reaction	1 min	RT, 30 min	RT, 30 min	RT, 30 min	RT, 30 min	RT, 30 min	RT, 30 min
Histofine		Anti-mouse	Anti-rabbit	Anti-mouse	Anti-mouse	Anti-mouse	Anti-rabbit
Reaction		RT, 30 min	RT, 30 min	RT, 30 min	RT, 30 min	RT, 30 min	RT, 30 min
AEC reaction time		20 min	20 min	10 min	40 min	20 min	20 min

		Round 7	Round 8	Round 9	Round 10	Round 11	Round 12-1	Round 12-2 #
Primary Ab	GATA-3	Foxp3	PD-L1	CD20	CD45	EpCAM		p16
Supplier	BD Bioscience	eBioscience	Cell Signaling	Santa Cruz	Thermo Scientific	US Biological		Ventana
Clone/Product#	L50-823	236A/E7	E1L3N	0.N.85	H130	6k161		E6H4
Concentration	1:100	1:40	1:100	1:1000	1:100	1:500		Prediluted
Reaction	RT, 30 min	RT, 30 min	RT, 60 min	RT, 30 min	RT, 30 min	RT, 30 min		RT, 30 min
Histofine	Anti-mouse	Anti-mouse	Anti-rabbit	Anti-mouse	Anti-mouse	Anti-rabbit		Anti-mouse
Reaction	RT, 30 min	RT, 30 min	RT, 30 min	RT, 30 min	RT, 30 min	RT, 30 min		RT, 30 min
AEC reaction time	40 min	20 min	40 min	20 min	40 min	10 min		20 min

Myeloid biomarker panel

		Round 1	Round 2	Round 3	Round 4	Round 5	Round 6
Primary Ab	Hematoxylin	Tryptase	CD68	CSF1R	DC-SIGN	CD66b	CD83 §
Supplier	Dako	Abcam	Abcam	Abcam	Santa Cruz Biotech	eBioscience	Abcam
Clone/Product#	S3301	AA1	PG-M1	SP211	DC-28	G10F5	1H4b
Conc		1:20,000	1:50	1:150	1:100	1:600	1:40
Reaction	1 min	RT, 30 min	RT, 30 min	RT, 30 min	RT, 30 min	RT, 30 min	RT, 30 min
Histofine		Anti-mouse	Anti-mouse	Anti-rabbit	Anti-mouse	Anti-mouse	Anti-mouse
Reaction		RT, 30 min	RT, 30 min	RT, 30 min	RT, 30 min	RT, 30 min	RT, 30 min
AEC reaction time		20min	20min	10min	20min	20min	20min

		Round 7	Round 8	Round 9	Round 10	Round 11	Round 12-1	Round 12-2 #
Primary Ab	CD163	MHC class II ¶	PD-L1	CD3/20/56	CD45	EpCAM		p16
Supplier	Thermo Scientific	Novus Biological	Cell Signaling	*	Thermo Scientific	US Biological		Ventana
Clone/Product#	10D6	SPM288	E1L3N	*	H130	6k161		E6H4
Conc	1:100	1:100	1:100	*	1:100	1:500		Prediluted
Reaction	RT, 30 min	RT, 30 min	RT, 60 min	RT, 30 min	RT, 30 min	RT, 30 min		RT, 30 min
Histofine	Anti-mouse	Anti-mouse	Anti-rabbit	**	Anti-mouse	Anti-rabbit		Anti-mouse
Reaction	RT, 30 min	RT, 30 min	RT, 30 min	RT, 30 min	RT, 30 min	RT, 30 min		RT, 30 min
AEC reaction time	20min	10min	40min	20min	40 min	10 min		20 min

Functional biomarker panel

		Round 1 †	Round 2	Round 3	Round 4	Round 5	Round 6
Primary Ab	Hematoxylin	CD4	CD3	PD-1	Ki67	CD8	Eomes (Tbr2)
Supplier	Dako	Thermo Scientific	Thermo Scientific	Abcam	Abcam	Thermo Scientific	EMD Millipore
Clone/Product#	S3301	4B12	SP7	NAT105	SP6	C8/144B	AB2283
Conc		1:25	1:150	1:50	1:500	1:50	1:1000
Reaction	1 min	RT, 30min	RT, 30min	RT, 30min	RT, 30min	RT, 30min	RT, 30min
Histofine		Anti-mouse	Anti-rabbit	Anti-mouse	Anti-rabbit	Anti-mouse	Anti-rabbit
Reaction		RT, 30min	RT, 30min	RT, 30min	RT, 30min	RT, 30min	RT, 30min
AEC reaction time		20min	20min	20min	20min	20min	20min

		Round 7	Round 8	Round 9	Round 10	Round 11
Primary Ab	IDO	Granzyme B	CD68	T-bet	CD45	
Supplier	EMD Millipore	Sigma Aldrich	Abcam	Santa Cruz Biotech	Thermo Scientific	
Clone/Product#	1F8.2	EP230	PG-M1	sc-21003	H130	
Conc	1:100	1:100	1:50	1:100	1:50	
Reaction	RT, 30min	RT, 30min	RT, 30min	RT, 30min	RT, 30min	
Histofine	Anti-mouse	Anti-rabbit	Anti-mouse	Anti-rabbit	Anti-mouse	
Reaction	RT, 30min	30 min	RT, 30min	RT, 30min	RT, 30min	
AEC reaction time	20min	20min	20min	20min	40min	

Round 12 was utilized only for HNSCC-TMA analysis. No antibody stripping protocol was applied between Round 12-1 and 12-2.

§ This antibody was discontinued by the supplier. We confirmed anti-DC-LAMP antibody (1010E1.01, Novus Biological, 1:100) & anti-rat Histofine (414311F) & 30-min AEC work as an alternative of a mature DC marker for future studies.

¶ This antibody was discontinued by the supplier. We confirmed anti-MHC class II antibody (EPR11226, abcam, 1:5000) & anti-rabbit Histofine (414141F) & 20-min AEC work as an alternative of MHC class II for future studies.

* CD3(SP7), 1:150; CD20(0.N.85), 1:1,000; CD56(123C3), 1:25

** Anti-Mouse for 30 min, Anti-Rabbit for 30 min

† Antigen retrieval was performed by Tris-EDTA (10 mM Tris Base, 1 mM EDTA and 0.05% Tween-20, pH 9.0).

Table S2 in reference to Figure 4. Patient and disease characteristics in HNSCC TMA

Features		All patients N = 38	HPV-positive N = 21	HPV-negative N =17
Gender				
	Male	29	18	11
	Female	9	3	6
Age				
	< 60	14	8	6
	60–80	23	13	10
	> 80	1	0	1
T stage				
	1–2	36	21	15
	3–4	2	0	2
N stage				
	0	20	8	12
	1–3	18	13	5
M stage				
	0	38	21	17
	1	0	0	0
Stage				
	I–II	18	8	10
	III–IV	20	13	7
Smoking history				
	Never	10	7	3
	Ever	28	14	14
Alcohol consumption				
	Absent	22	14	8
	Present	13	7	6
	Unknown	3	0	3

Table S3 in reference to Figure 5. Patient and disease characteristics in GVAX-treated PDAC.

Features	All patients N = 24	
Gender		
	Male	11
	Female	13
Resection margin		
	+ve	4
	-ve	20
Tumor size		
	≥ 2 cm	22
	< 2 cm	2
Lymph node status		
	Positive	20
	Negative	4
Histologic grade		
	Grade 1-2	19
	Grade 3-4	5

SUPPLEMENTAL EXPERIMENTAL PROCEDURES

Clinical samples and TMA construction

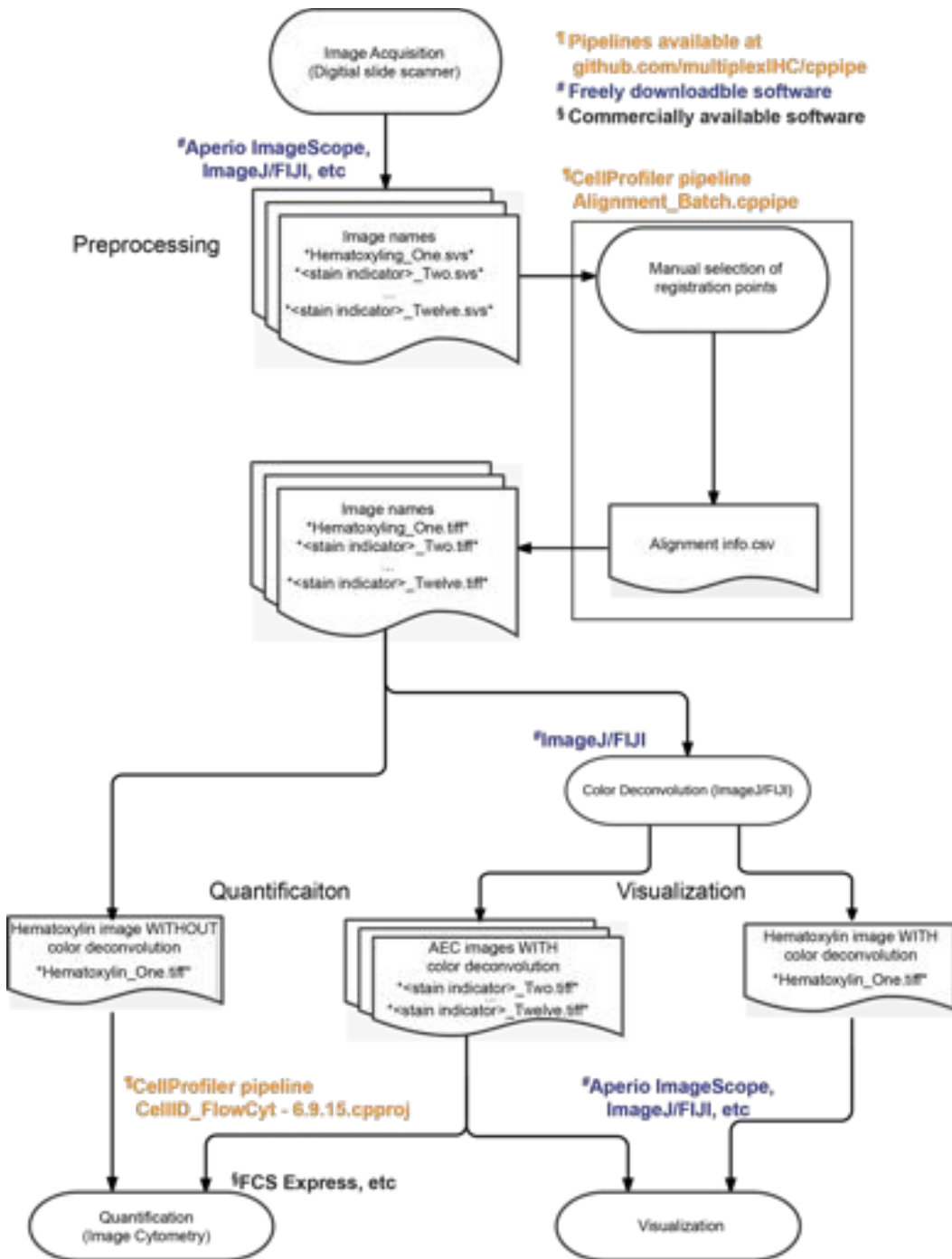
Human FFPE samples of HNSCC were obtained from the Oregon Health and Science University (OHSU) Knight Bioblibrary, and the OHSU Department of Dermatology research repository. FFPE surgical specimens were obtained from a total of 38 patients with previously untreated oropharyngeal squamous cell carcinoma, and were used to create a TMA for analysis. All HNSCC samples were reviewed by a head and neck pathologist (D.A.S) to select representative tissue with dense, non-necrotic tumor. As control, a total of 10 adult palatine and lingual tonsillectomy specimen removed for benign, non-inflammatory indications (i.e. obstructive sleep apnea) were included in the TMA. The TMA was created using an automated microarrayer (3D Histech TMA Master; Budapest, Hungary), which took 2 mm cores from the selected area of the donor block and placed them into an array on the recipient block. All HNSCC tumors were staged according to the 7th edition AJCC/UIC TNM classification and cohort characteristics are shown in **Table S2**. HPV-status was determined by p16 staining and/or by quantitative PCR when available. Two cases of benign tonsillectomy specimen were excluded due to insufficient amount of tissue in the TMA. A total of 24 human PDAC tumor specimens with presence of intratumoral lymphoid aggregates were obtained from our previous study wherein allogeneic GM-CSF-secreting pancreatic tumor vaccine (GVAX) was administered intradermally either alone or in combination with immune modulatory doses of cyclophosphamide as neoadjuvant treatment for patients with resectable PDAC (NCT00727441, **Table S3**) (Lutz et al., 2014).

Sequential immunohistochemistry and image acquisition

Sections (5 µm) of FFPE tissues were placed in a 60°C heat chamber for 30 min, deparaffinized with xylene, and rehydrated in serially graded alcohols to distilled water. Slides were stained by hematoxylin (S3301, Dako) for 1 min, mounted with TBST buffer (0.1 M TRIS-HCl, pH 7.5, 0.15 M NaCl plus 0.05% Tween-20), and coverslipped with Signature Series Cover Glass (12460S, Thermo Scientific), followed by whole tissue scanning using an Aperio ImageScope AT (Leica Biosystems) at 20x magnification. After decoverslipping slides with 1.0 min. agitation in TBST, peroxidase activity was blocked by 0.6% hydrogen peroxidase in methanol for 30 min, and slides were subjected to heat-mediated antigen retrieval immersed in citrate buffer (pH 6.0) or Tris-EDTA (10 mM Tris Base, 1.0 mM EDTA and 0.05% Tween-20, pH 9.0) for 15 min. Then, sequential immunohistochemistry consisting of iterative cycles of staining, scanning, and antibody/chromogen stripping was performed according to a modified protocol based on previous reports (Glass et al., 2009; Lan et al., 1995; Tramu et al., 1978). After a protein blocking step with 5.0% goat serum, 2.5% BSA, and 0.1% Tween-20, unlabeled primary antibodies were added to sections at the indicated dilution shown in **Table S1**. After washing in TBST buffer, slides were visualized with either an anti-mouse or anti-rabbit Histofine Simple Stain MAX PO horseradish peroxidase-conjugated polymer (Nichirei Biosciences Inc.), followed by peroxidase detection with AEC for the indicated incubation time specified in **Table S1**. Cover slipping, whole tissue scanning, and decoverslipping were performed as described above. Following chromogenic destaining in an alcohol gradient, antibodies were stripped by a 15 min low power microwave heat treatment following high power boiling in Antigen Retrieval Citra Solution (BioGenex). Slides were then restained sequentially in the indicated order shown in **Table S1**.

Image processing and analysis

The digital image workflow encompasses three steps: image preprocessing, visualization, and quantitative image analysis as shown in below.



A flowchart showing digital image processing workflow in multiplex IHC. Following image acquisition by digital slide scanner, images are subjected to three steps, consisting of preprocessing, quantification and visualization. Software required for this workflow is indicated as CellProfiler pipelines available at <https://github.com/multiplexIHC/cppipe> (§), free or open-source software (#), and commercially available software (§).

Image preprocessing and selection of ROI were conducted as described below. Since iteratively digitized images need to be precisely co-registered so that cell features overlap down to a single pixel level, coregistration of images was performed using a CellProfiler Version 2.1.1 pipeline, “Alignment_Batch.cppipe” developed by VA and RNB. The

pipeline is available under GPLv2 (a widely used free software license) at <https://github.com/multiplexIHC/cppipe>. Pseudocodes for algorithms used are available in **Supplementary Note 2**. Based on a small number of manually selected single structures such as cells, vessels, and edges of tissues, the pipeline calculates global vertical and horizontal offsets for each image relative to the hematoxylin stained image. Using these coordinate ranges and the co-registration offsets, we extract a set of non-compressed TIFF images for each ROI that are aligned across the single-marker images, and ready for quantitative analysis and visualization. In the HNSCC TMA analysis, each ROI was selected from a total area of each single tissue core. In the PDAC surgical specimen analysis, a heat map of CD45⁺ cell density in the whole-slide digital images was generated based on hematoxylin and CD45-IHC images. Then, the heat map was utilized for selection of three rectangle ROIs within intratumoral high CD45-density area (approximately 6.25 mm², or less if analyzable cancerous area is smaller than 3.0 x 6.25 mm²) (**Figure S6F**).

Visualization was performed via conversion of co-registered images to pseudo-colored single-marker images in ImageJ Version 1.48 (Schneider et al., 2012): following coregistration, exported images were processed using an ImageJ plugin, Color_Deconvolution (www.mecourse.com/landinig/software/software.html) for AEC and hematoxylin signal separation¹³. Following pixel histogram optimization, images were then inverted and converted to gray-scale, followed by pseudo-coloring in ImageJ and ImageScope (Leica Biosystems) as described previously (Gunderson et al., 2015).

Single cell-based segmentation and quantification of staining intensity was performed using an automated image segmentation pipeline "CellID_FlowCyt - 6.9.15.cpproj" (developed by VA and RNB) using CellProfiler Version 2.1.1. The pipeline is available under GPLv2 at <https://github.com/multiplexIHC/cppipe>. Pseudocodes for algorithms used are available in **Supplementary Note 3**. This customized pipeline used several AEC-stained images for assessment of signal intensities, and one hematoxylin-stained image for cell segmentation. First, individual RGB channels were extracted from the hematoxylin-stained image. Next, pixel intensities for images were inverted to optimize the algorithm's ability to detect cells. Cell segmentation of the hematoxylin-stained image was then performed using a built-in watershed segmentation algorithm as described previously (Wählby et al., 2004). Prior to segmentation, a built-in thresholding method was utilized to identify local intensity maxima and minima, as well as to differentiate foreground from background pixels, as described previously (Padmanabhan et al., 2010). The nature of multiplex staining allows segmentation results (referred to as "objects") to be used as templates for staining quantification of serially scanned AEC images. The color channel specific to AEC staining was extracted from each AEC-stained image. Using objects from the watershed segmentation, cell coordinates were overlaid onto these AEC channels, thus locating each cell on the biomarker-stained images. Subsequently, measurements of pixel intensity were extracted and recorded. CellProfiler also measured 26 different area and shape features of cells in the image. A color map was then constructed of all identified cells by assigning a number to each pixel within each individual cell, and saved for image cytometry analysis. Finally, all pixel intensity and shape-size measurements were saved to a file format compatible with flow and image cytometry data analysis software, FCS Express 5 Image Cytometry Version 5.01.0029 (De Novo Software).

Pseudocode for image coregistration

```
# The inputs are the script, and an array of the image files (in most cases 12 total). It is assumed the first image is H&E, and is only used for alignment and segmentation

script, image1, image2, image3, image4, image5, image6, image7, image8, image9, image10, image11, image12 =
inputs

"""" Alignment """"
```

```

# The implemented alignment algorithm aligns all images to the first image in the list.

# Displays each image, in which the user must select a common point

def find_offsets(all_image_files):

    file1 = all_image_files[0]

    # Reference coordinates to be compared to each other image's coordinates

    file1_coordinates = []

    # X and y offsets. Image 0 (file1) has an offset of 0,0 because it's the reference image. All other images are
    aligned to it.

    offsets = [ (0,0) ]

    # When the user right clicks in the graph, it adds the coordinates to the coordinate list. When the window is
    closed, the script continues

    # IMPORTANT: Coordinate lists must be same length.

    def onclick(event, coordinate_list):

        coordinate_list.append( (event.x, event.y) )

    figure1.showimage(file1)

    figure1.connect("right_click_event", onclick(file1_coordinates))

    figure1.show()

    # Iterate through all images (besides first "reference" image)

    for x in range(1, len(all_image_files)):

        filex_coordinates = []

        while len(filex_coordinates) != len(file1_coordinates):

            figure1.showimage(all_image_files[x])

            figure1.connect("right_click_event", onclick(filex_coordinates))

            figure1.show()

```

```
    # Offset compared to reference image (file1). Find difference between reference image and current image points.
```

```
    x_offset = int(sum(filex_coordinates[a][0] - file1_coordinates[a][0] for a in range(0, len(filex_coordinates))))/len(filex_coordinates))
```

```
    y_offset = int(sum(filex_coordinates[a][1] - file1_coordinates[a][1] for a in range(0, len(filex_coordinates))))/len(filex_coordinates))
```

```
    # Add this image's coordinates to offsets array
```

```
    offsets.append( (x_offset, y_offset) )
```

```
return offsets
```

Pseudocode for cell segmentation and signal quantification

```
# The inputs are the script, and an array of the image files (in most cases 12 total). It is assumed the first image is H&E, and is only used for alignment and segmentation
```

```
script, image1, image2, image3, image4, image5, image6, image7, image8, image9, image10, image11, image12 = inputs
```

```
""" Segmentation and Data Collection """
```

```
# This code assumes the images have been aligned
```

```
max_cell_size = 100
```

```
min_cell_size = 10
```

```
# Only segments one image, and returns labels to be applied to all images after alignment
```

```
def segment(image):
```

```
    # Watershed segmentation based on a distance or gradient transform
```

```
    img = image.rgb2gray()
```

```
    #distance = distance_transform(img)
```

```
    gradient = gradient(img)
```

```
    local_maxi = find_local_maxima(gradient)
```

```
    markers = label(local_maxi)
```

```

labels = watershed(-gradient, markers, mask=image)

# Remove cells that are too big or too small
temp_props = regionprops(labels, image)
for cell in temp_props:
    if cell['area'] < min_cell_size or cell['area'] > max_cell_size:
        labels[labels == cell['label']] = 0

return labels

# Collect stain data from all images except first (assumes first is H&E)
def collect_data(all_image_files, labels):
    # Make dataframe to store protein intensities
    save_data = pd.DataFrame( col1=labels['label'], col1_name='Cells' )
    # Record label numbers, in order
    save_data['Labels'] = (x['label'] for x in regionprops(labels))

    # In each image, measure the AEC level of each label
    for x in range(1, len(all_image_files)):
        add_data = []
        for cell in regionprops(labels):
            # Access pixels of each label, overlay the image onto pixels, and record normalized RGB
            intensities = image[cell['label']]
            # These RGB values are normalized based on AEC staining (3-amino-9-ethylcarbazole). Values
            vary based on staining method

```

```

                                add_data.append(a['pixels'].read_pixels( mask=all_image_files[x], normalize=(0.274, 0.679,
0.680) ))

                                save_data['Image_' + x + '_AEC'] = add_data

# Save data is organized as a pandas dataframe of rows and columns.

# The first column is the label count for individual (1 to [number of labels])

# The 2nd-12th columns are the AEC intensity values of each label (cell) on each image.

save_data.io.save("Image_Cytometry_Results")

# Make arrays of all input images

all_images = [image1.asarray, image2.asarray, image3.asarray,

                                image4.asarray, image5.asarray, image6.asarray,

                                image7.asarray, image8.asarray, image9.asarray,

                                image10.asarray, image11.asarray, image12.asarray]

# Dictionary of image offsets

image_offsets = []

# Find offsets

image_offsets = find_offsets(all_images)

# Align images based on offsets

for x in range(0, len(image_offsets))

    all_images[x] = realign_pixels( all_images[x], image_offsets[x] )

# Now that images are aligned, segment cells in H&E image and collect data

collect_data( all_images, segment(all_images[0]) )

```

REFERENCE FOR SUPPLEMENTAL EXPERIMENTAL PROCEDURES

- Glass, G., Papin, J.A., and Mandell, J.W. (2009). SIMPLE: a sequential immunoperoxidase labeling and erasing method. *J Histochem Cytochem* 57, 899-905.
- Gunderson, A.J., Kaneda, M.M., Tsujikawa, T., Nguyen, A.V., Affara, N.I., Ruffell, B., Gorjestani, S., Liudahl, S.M., Truitt, M., Olson, P., *et al.* (2015). Bruton's Tyrosine Kinase (BTK)-dependent immune cell crosstalk drives pancreas cancer. *Cancer Discov* 6, 270-285.
- Lan, H.Y., Mu, W., Nikolic-Paterson, D.J., and Atkins, R.C. (1995). A novel, simple, reliable, and sensitive method for multiple immunoenzyme staining: use of microwave oven heating to block antibody crossreactivity and retrieve antigens. *Journal of Histochemistry & Cytochemistry* 43, 97-102.
- Lutz, E.R., Wu, A.A., Bigelow, E., Sharma, R., Mo, G., Soares, K., Solt, S., Dorman, A., Wamwea, A., and Yager, A. (2014). Immunotherapy Converts Nonimmunogenic Pancreatic Tumors into Immunogenic Foci of Immune Regulation. *Cancer Immunology Research* 2, 616-631.
- Padmanabhan, K., Eddy, W.F., and Crowley, J.C. (2010). A novel algorithm for optimal image thresholding of biological data. *J Neurosci Methods* 193, 380-384.
- Schneider, C.A., Rasband, W.S., and Eliceiri, K.W. (2012). NIH Image to ImageJ: 25 years of image analysis. *Nat Methods* 9, 671-675.
- Tramu, G., Pillez, A., and Leonardelli, J. (1978). An efficient method of antibody elution for the successive or simultaneous localization of two antigens by immunocytochemistry. *J Histochem Cytochem* 26, 322-324.
- Wählby, C., SINTORN, I.M., Erlandsson, F., Borgefors, G., and Bengtsson, E. (2004). Combining intensity, edge and shape information for 2D and 3D segmentation of cell nuclei in tissue sections. *J Microsc* 215, 67-76.